95-0002

VLF Far-Field Radiation from a Linear Dipole Antenna Immersed in a Plasma: Baseline Model for DSX

G.P. Ginet

15 June 2020

Lincoln Laboratory
MASSACHUSETTS INSTITUTE OF TECHNOLOGY
LEXINGTON, MASSACHUSETTS

This material is based upon work supported under Air Force Contract No. FA8702-15-D-0001.

This report is the result of studies performed at Lincoln Laboratory, a federally funded research and development center operated by Massachusetts Institute of Technology. This material is based upon work supported under Air Force Contract No. FA8702-15-D-0001. Any opinions, findings, conclusions or recommendations expressed in this material are those of the author(s) and do not necessarily reflect the views of the U.S. Air Force.

Massachusetts Institute of Technology
Lincoln Laboratory

VLF Far-Field Radiation from a Linear Dipole Antenna Immersed in a Plasma: Baseline Model for DSX

G.P. Ginet
Group 95

95-0002

15 June 2020

This material is based upon work supported under Air Force Contract No. FA8702-15-D-0001.

Lexington Massachusetts

This page intentionally left blank.

ABSTRACT

One of the prime objectives of the Demonstrations and Science Experiment (DSX) satellite mission is to determine the efficiency of injecting power into the magnetosphere at Very Low Frequencies (VLF) from an in-situ dipole antenna. A baseline VLF antenna radiation model for DSX has been developed using the stationary phase, far-field approximation to obtain a solution to the Green's function for the electric and magnetic fields driven by the antenna current in the limit of cold-plasma linear response theory. Estimates of the wave vectors and Poynting flux are output on the surface of a sphere of constant radius assuming a homogeneous plasma. The input antenna currents can either be specified from the data or derived from an impedance relation with the antenna voltages. An example impedance function, that of Balmain [11], is given and results generated for parameters typical of the DSX plasma environment. The intent of the model is to serve as a baseline linear model to which DSX data can be compared, and the differences used to guide model improvement.

This page intentionally left blank.

1. INTRODUCTION

Antennas immersed in plasma behave very differently than antennas in vacuo when the operating frequencies are in the range of the resonant frequencies of the media, e.g. the electron plasma, electron cyclotron or lower-hybrid frequencies, as is the case for Very Low Frequency (VLF, 3 kHz–30 kHz) emitters in the inner magnetosphere. The motion of free charges in the plasma can (a) create sheaths that dominate the antenna impedance and store significant amounts of energy; (b) introduce additional currents whose time rate-of-change contributes to the radiated power potentially out of phase with the antenna currents; and (c) absorb energy from the wave transforming it into collective plasma motions. Furthermore, even if all of the above effects were not significant the plasma is an anisotropic dielectric supporting both propagating and non-propagating modes with a complex index of refraction function depending on plasma density, magnetic field strength, wave-vector direction and frequency. The primary goal of the VLF transmitter and receiver comprising the Wave-Particle Interactions Experiment (WPIx) on the Demonstrations and Science Experiment (DSX) spacecraft is to collect the data needed to understand the aforementioned processes and establish a realistic model of the far-field radiation efficiency.

Over the last several decades the behavior of an antenna immersed in plasma has been modeled a number of ways spanning the range from linear response theory in cold plasma [1–3] to one-dimensional circuit models including sheath effects [4–7], to full three-dimensional hybrid particle-in-cell/fluid simulations [8–10]. The purpose of the work reported here is to develop a baseline model for the DSX VLF far-field radiation which can be used to estimate the distribution of the Poynting flux and wave-vector on a spherical surface at some distance from the satellite. Values of this sphere can then be used as initial conditions for ray-tracing which, in turn, can estimate where and at what amplitude injected VLF power propagates into the magnetosphere. The model is meant to be simple and robust, following the well-traversed path of linear response theory with a fixed current source and the method of stationary phase, and is therefore limited. Non-linear effects, such as the behavior near resonance, and antenna mutual and plasma coupling effects are included only in an ad-hoc manner. Components of the baseline model can be improved or discarded as the DSX experiment and analysis shed increasing light on the relevant processes.

This report describes the model in a level of detail that should allow for straightforward independent implementation into numerical algorithms. In Section 2 the dipole antenna model, the wave propagation regime relevant to DSX and a stationary phase solution for the linear VLF propagation model are presented. Included is a description of the method used to handle behavior near the resonance angle. The solutions are a function of the dipole antenna currents which can be determined directly from DSX antenna measurements or, as outlined in Section 3, estimated from an antenna impedance model such as that of Balmain [11]. Some example solutions are presented in Section 4 and a summary is given in Section 5. Appendix A contains the basic cold plasma dispersion relations underlying the model.

This page intentionally left blank.

2. VLF FAR-FIELD ANTENNA RADIATION MODEL

2.1 DIPOLE ANTENNA MODEL

The physical model for a linear dipole antenna with length d and radius a is shown in Figure 1. Cartesian coordinates (x, y, z) and spherical coordinates $(r, \theta_{obs}, \phi_{obs})$ represent the physical space of the observer. A background magnetic field $\mathbf{B_0} = \mathbf{B_0 e_z}$ is assumed along the z axis and the dipole is oriented at an angle β_{ant} with respect to $\mathbf{B_0}$ in the $x - z$ plane. An input voltage V_0 drives a current into the antenna with a value I_0 at the dipole terminals and a fixed profile along the dipole arms.

The DSX Y-boom transmit dipole antenna has $d = 80$ m and is composed of 3 wires each 0.4 mm in diameter (26 AWG) in an equilateral triangle cross-section configuration with sides of length 20 cm. In the DSX plasma environment (see Section 2.3 and Section 3) the three wires are separated by less than a Debye length and are strongly electromagnetically coupled suggesting that an effective antenna radius of $a_{eff} = 0.12$ m, i.e., distance from the center of the triangle to the wires, might be a reasonable approximation to estimate plasma coupling. However, for the far-field radiation calculations $r_{obs} >> d$ and a, so the limit $a = 0$ is a good approximation.

For the far-field estimation a fixed, linear current density profile of the following form will be assumed,

$$\begin{aligned} \mathbf{J}(\mathbf{x}, t) &= I_0(t) \left(1 - \frac{|u|2}{d}\right) \delta(v)\delta(y), \quad |u| \leq \frac{d}{2}, \\ &= 0, \quad |u| > \frac{d}{2}, \end{aligned} \tag{1}$$

where,

$$\begin{aligned} u &= z \cos\beta_{ant} + x \sin\beta_{ant}, \\ v &= z \sin\beta_{ant} - x \cos\beta_{ant}, \end{aligned} \tag{2}$$

and $a = 0$. All quantities varying in time t (e.g., the current density $\mathbf{J}(\mathbf{x}, t)$) are assumed to have a harmonic variation which can be expressed as a single Fourier mode (e.g., $\hat{\mathbf{J}}(\mathbf{x}, \omega)$),

$$\mathbf{J}(\mathbf{x}, t) = \frac{1}{2}\left[\hat{\mathbf{J}}(\mathbf{x}, \omega)\exp\{j\omega t\} + \hat{\mathbf{J}}^*(\mathbf{x}, \omega)\exp\{j\omega t\}\right] = \Re\left[\hat{\mathbf{J}}(\mathbf{x}, \omega)\exp\{j\omega t\}\right] \tag{3}$$

where f is the frequency and $\omega = 2\pi f$. Furthermore, the spatial variation will be represented as a Fourier integral of the form,

$$\hat{\mathbf{J}}(\mathbf{x}, \omega) = \frac{1}{(2\pi)^3}\int_{-\infty}^{+\infty} d^3k\ \tilde{\mathbf{J}}(\mathbf{k}, \omega)\exp\{-j\mathbf{k}\cdot\mathbf{x}\} \tag{4}$$

with,

$$\tilde{\mathbf{J}}(\mathbf{k}, \omega) = \int_{-\infty}^{+\infty} d^3x\ \hat{\mathbf{J}}(\mathbf{x}, \omega)\exp\{j\mathbf{k}\cdot\mathbf{x}\} \tag{5}$$

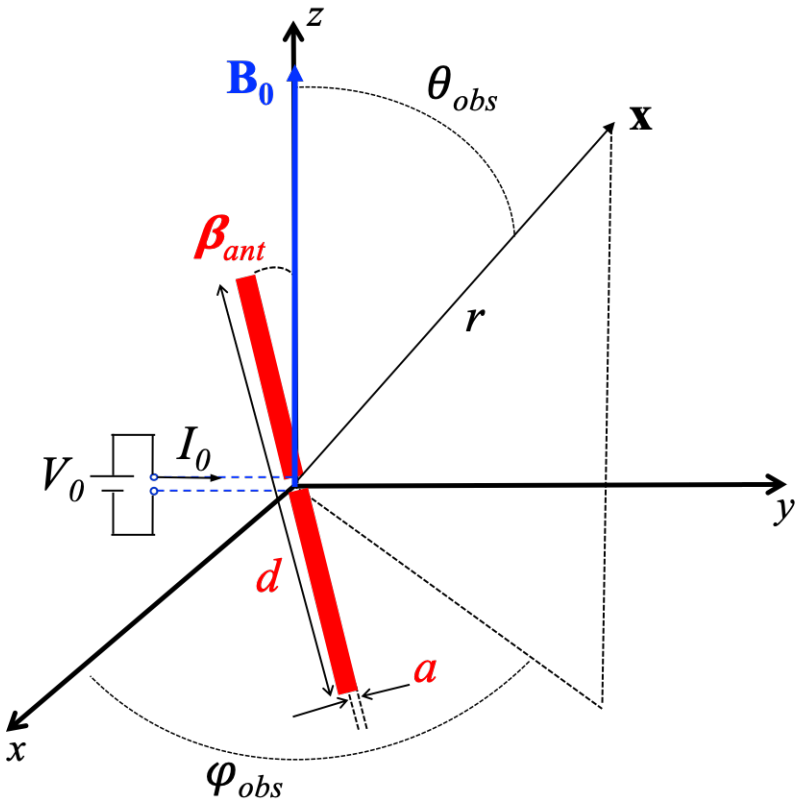

Figure 1. Linear dipole antenna model.

where $\mathbf{k} = (k_x, k_y, k_z)$ is the wave vector. The linear current density profile (Eq. 1) can then be written,

$$\tilde{J}_x(\mathbf{k},\omega) = \frac{8\hat{I}_0 \sin\beta_{ant}}{d\left(k_x \sin\beta_{ant} + k_z \cos\beta_{ant}\right)^2} \sin^2\left[\frac{\left(k_x \sin\beta_{ant} + k_z \cos\beta_{ant}\right) d}{4}\right], \tag{6}$$

$$\tilde{J}_y(\mathbf{k},\omega) = \frac{8\hat{I}_0 \cos\beta_{ant}}{d\left(k_x \sin\beta_{ant} + k_z \cos\beta_{ant}\right)^2} \sin^2\left[\frac{\left(k_x \sin\beta_{ant} + k_z \cos\beta_{ant}\right) d}{4}\right]. \tag{7}$$

2.2 WAVE MODES IN THE DSX PLASMA REGIME

The DSX satellite is in a 6000 km x 12,000 km, 42° inclination orbit and spends most of its time inside the Earth's plasmasphere with intermittent excursions outside the plasmasphere. Figure 2 plots a number of characteristic frequencies important in cold plasma theory (Appendix A) for a day in the life of DSX—in particular 21 September 2019. Estimates of the plasma densities and magnetic field strengths needed to compute the characteristic frequencies are obtained from the

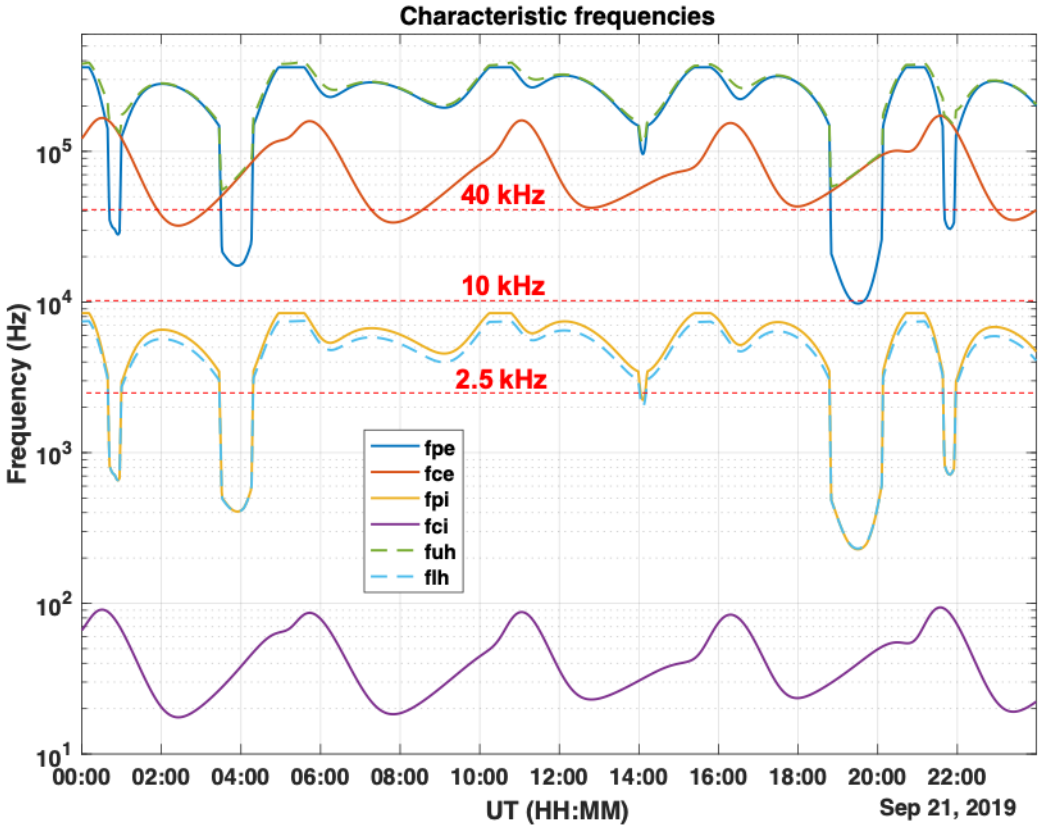

Figure 2. Characteristic frequencies (see legend and Appendix A) as a function of time for a day in the life of DSX (21 September 2019). Red dotted lines indicate the minimum (2.5 kHz), an intermediate (10 kHz) and the maximum (40 kHz) DSX broadcast frequencies. A single orbit is about 5.27 hours.

Carpenter-Anderson plasmasphere model [12] and the International Geophysical Reference Field [13], respectively, as output by the DSX extended ephemeris [14]. DSX transmits in the range 2.5–40 kHz, as indicated by the red dashed lines in the figure. An intermediate transmit frequency at 10 kHz is also shown. The sharp dips in the electron and ion plasma frequencies are times when DSX is outside the plasmasphere, and the flattened regions in the plasma frequency profiles are due to the saturated density in the Carpenter-Anderson model.

Paramount to achieving far-field radiation is that the index of refraction η at the propagation frequency be a real number. In the limit of cold plasma theory, this is equivalent to $\eta^2 > 0$ where η^2 is given by the dispersion relation Eq. (A.39). In Figure 3 the square of the index of refraction is plotted as a function of time for the same day in the life of DSX as shown in Figure 2. Both the plus (blue) and minus (red) roots of the dispersion relation are shown for the the minimum (2.5 kHz) , intermediate (10 kHz) and the maximum (40 kHz) DSX transmit frequencies. The left-hand column (Figures 3a–c) are solutions of the dispersion relation with the wave vector parallel

to the magnetic field ($\theta = 0$) while the right-hand column are the solutions when the wave vector is perpendicular to the magnetic field ($\theta = \pi/2$).

There are a variety of possible wave propagation modes possible depending on frequency and wave-vector angle. Though the broadcast frequency can be chosen by the experimenter, the wave-vector angles at which the power propagates away from the antenna are determined by the plasma response. The objective of the DSX mission is to broadcast in the whistler regime, which is represented by the curves shown in Figure 3b and 3e. It is the minus root of the dispersion relation which propagates inside the plasmasphere (e.g., the red curve with $\eta^2 > 0$ in Figure 3b for $\theta = 0$) for wave-vector angles less than a critical resonance angle, beyond which no modes propagate (e.g., the red curve having $\eta^2 < 0$ in Figure 3e for $\theta = \pi/2$). An enhanced resolution of the plot of Figure 3b and 3e for a time when DSX is outside of the plasmasphere is shown in Figure 4a and 4b, respectively. In this case, the plus root propagates for all wave-vector angles while the minus root exhibits a cutoff response similar to its behavior inside the plasmasphere. For the remainder of this report analysis will focus on the minus root of the dispersion relation in the "whistler regime", as exemplified in Figure 3a and 3b.

2.3 LINEAR RESPONSE MODEL FOR THE ELECTROMAGNETIC FIELDS

The matrix wave equation for the electric field in Fourier space with a fixed current source is given in Appendix A (Eq. A.10) and can be inverted to yield,

$$\tilde{\mathbf{E}} = j\omega\mu_0 \left(\mathbf{kk} - k^2\mathbf{I} + \omega^2\mu_0\boldsymbol{\epsilon}\right)^{-1} \cdot \tilde{\mathbf{J}}_{ext} \ . \tag{8}$$

After some manipulation the matrix in the above equation can be written as,

$$\left(\mathbf{kk} - k^2\mathbf{I} + \omega^2\mu_0\boldsymbol{\epsilon}\right)^{-1} = \frac{\boldsymbol{\Lambda}}{k_0^2\alpha\left(k^2 - k_+^2\right)\left(k^2 - k_-^2\right)} \ , \tag{9}$$

where,

$$\boldsymbol{\Lambda} = k^4\mathbf{nn} - k^2k_0^2\mathbf{L} + k_0^4\mathbf{W} \ , \tag{10}$$

$$\alpha(\theta) = \bar{\epsilon}_1 \sin^2\theta + \bar{\epsilon}_3 \cos^2\theta \ , \tag{11}$$

$$\frac{k_\pm^2}{k_0^2} = \frac{1}{2\alpha}\left\{\left(\bar{\epsilon}_1^2 - \bar{\epsilon}_2^2\right)\sin^2\theta + \bar{\epsilon}_1\bar{\epsilon}_3\left(1 + \cos^2\theta\right) \pm \left[\left(\bar{\epsilon}_1^2 - \bar{\epsilon}_2^2 - \bar{\epsilon}_1\bar{\epsilon}_3\right)^2\sin^4\theta + 4\bar{\epsilon}_2^2\bar{\epsilon}_3^2\cos^2\theta\right]^{1/2}\right\} \ , \tag{12}$$

with $k_0 = c/\omega$ the free-space wave vector, $\mathbf{n} = \mathbf{k}/k$ the unit vector in the $\mathbf{k}$ direction and,

$$\mathbf{L} = \begin{bmatrix} \bar{\epsilon}_1\left(n_x^2 + n_y^2\right) + \bar{\epsilon}_3\left(n_x^2 + n_z^2\right) & -j\bar{\epsilon}_2\left(n_x^2 + n_y^2\right) + \bar{\epsilon}_3 n_x n_y & \bar{\epsilon}_1 n_x n_z - j\bar{\epsilon}_2 n_y n_z \\ j\bar{\epsilon}_2\left(n_x^2 + n_y^2\right) + \bar{\epsilon}_3 n_x n_y & \bar{\epsilon}_1\left(n_x^2 + n_y^2\right) + \bar{\epsilon}_3\left(n_y^2 + n_z^2\right) & \bar{\epsilon}_1 n_y n_z + j\bar{\epsilon}_2 n_x n_z \\ \bar{\epsilon}_1 n_x n_z + j\bar{\epsilon}_2 n_y n_z & \bar{\epsilon}_1 n_y n_z - j\bar{\epsilon}_2 n_x n_z & \bar{\epsilon}_1\left(1 + n_z^2\right) \end{bmatrix} \ , \tag{13}$$

$$\mathbf{W} = \begin{bmatrix} \bar{\epsilon}_1\bar{\epsilon}_3 & -j\bar{\epsilon}_2\bar{\epsilon}_3 & 0 \\ j\bar{\epsilon}_2\bar{\epsilon}_3 & \bar{\epsilon}_1\bar{\epsilon}_3 & 0 \\ 0 & 0 & \bar{\epsilon}_1^2 - \bar{\epsilon}_2^2 \end{bmatrix} \ . \tag{14}$$

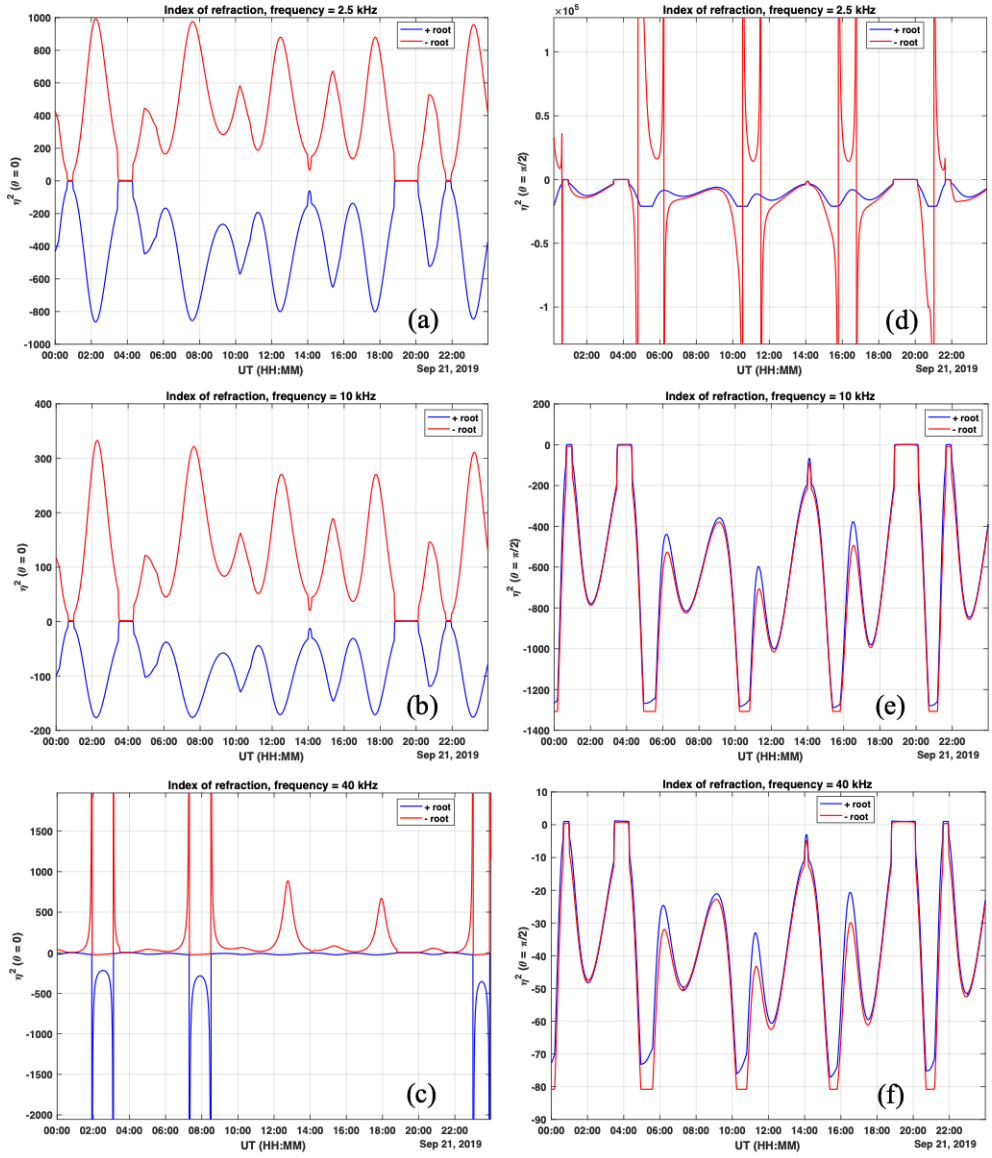

Figure 3. The square of the index of refraction (η^2) as a function of time for a day in the life of DSX (same as Figure 2) at 2.5 kHz (a,d), 10 kHz (b,e) and 40 kHz (c,f). The left (right) column is for wave-vectors aligned parallel (perpendicular) to the magnetic field.

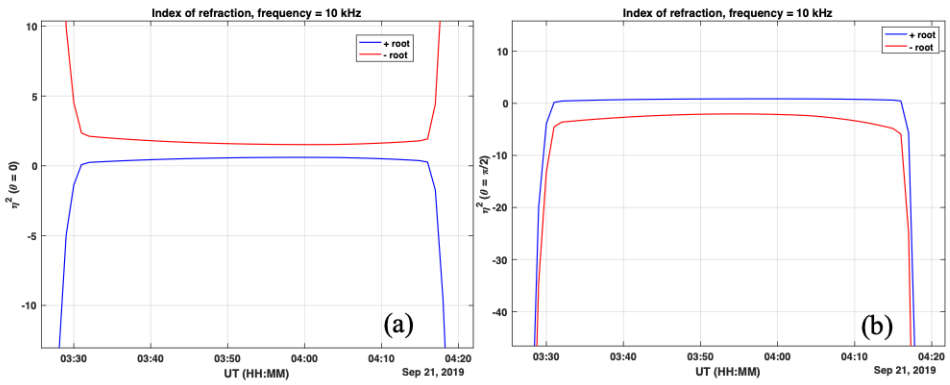

Figure 4. Enhanced resolution of Figure 3b and 3c for a portion of time when DSX is outside of the plasmasphere.

The inverse transform of Eq. (8) gives the solution to the wave equation in spatial coordinates,

$$\hat{\mathbf{E}}(\mathbf{x},\omega) = \frac{j\omega\mu_0}{(2\pi)^3}\int_{-\infty}^{+\infty} d^3k \;\exp\{-j\mathbf{k}\cdot\mathbf{x}\}\frac{\mathbf{\Lambda}\cdot\tilde{\mathbf{J}}_{ext}\left(\mathbf{k},\omega\right)}{k_0^2\alpha\left(k^2-k_+^2\right)\left(k^2-k_-^2\right)}\;. \tag{15}$$

Letting,

$$F(k,\theta,\phi) = \frac{\mathbf{\Lambda}\cdot\tilde{\mathbf{J}}_{ext}\left(\mathbf{k},\omega\right)}{k_0^2\alpha\left(k^2-k_+^2\right)\left(k^2-k_-^2\right)} \tag{16}$$

it can be shown that $F(k,\theta,\phi) = F(-k,\pi-\theta,\phi-\pi)$ and a solution to the wave equation can be written as,

$$\hat{\mathbf{E}}(\mathbf{x},\omega) = \frac{j\omega\mu_0}{(2\pi)^3}\int_0^{\pi/2} d\theta\sin\theta\int_0^{2\pi} d\phi\int_{-\infty}^{+\infty} dk k^2 \;\exp\{-jkr\cos\gamma\}F(k,\theta,\phi), \tag{17}$$

where,

$$\cos\gamma = \sin\theta\sin\theta_{obs}\cos\left(\phi-\phi_{obs}\right)+\cos\theta\cos\theta_{obs}\;. \tag{18}$$

The k integral in Eq. (17) can be computed analytically using Cauchy's integral theorem. To determine the poles in the whistler regime and which half-plane to close the semi-circle contour on as $|k|\to\infty$, the dispersion relation (Eq. A.39) can be expanded for the specific case $\theta = 0$ and $Z_e, Z_i << 1$. Noting that $\eta^2 = (ck/\omega)^2$, to first order in m_e/mi the four poles k_{1-4} are found to be ,

$$\begin{aligned} k_{1,2} &= \pm jk_+ \\ k_{3,4} &= \pm k_- - j\frac{Z_e\omega_{pe}^2}{2\omega_{ce}^2} \end{aligned} \tag{19}$$

where it is hereafter understood that $k_\pm$ corresponds to the magnitudes of the $\pm$ solutions of Eq. (12). Thus the contour integral is closed in the lower (upper) half-plane for $\cos\gamma < 0$ ($\cos\gamma > 0$)

to yield,

$$\begin{aligned}\hat{\mathbf{E}}(\mathbf{x},\omega) &= \frac{\omega\mu_0}{8\pi^2 k_0^2}\int_0^{\pi/2} d\theta \sin\theta \int_0^{2\pi} d\phi \frac{1}{\alpha\left(k_-^2 - k_+^2\right)} \\ &\times \Big[|k_-|\exp\{-jk_- r|\cos\gamma|\}\mathbf{\Lambda}\cdot\tilde{\mathbf{J}}_{ext}\left(\mathbf{k}_-,\omega\right) \\ &+|k_+|\exp\{-k_+ r|\cos\gamma|\}\mathbf{\Lambda}\cdot\tilde{\mathbf{J}}_{ext}\left(\mathbf{k}_+,\omega\right)\Big] \ . \end{aligned} \tag{20}$$

The case $\cos\gamma = 0$ is a set of measure zero in the (θ,ϕ) plane and will not contribute to the integral. In the far-field limit the evanescent term can be neglected giving the following expression for the electric field,

$$\hat{\mathbf{E}}(\mathbf{x},\omega) = \frac{\omega\mu_0}{8\pi^2 k_0^2}\int_0^{\pi/2} d\theta \sin\theta \int_0^{2\pi} d\phi \exp\{-jk_- r|\cos\gamma|\}\frac{k_-\mathbf{\Lambda}\cdot\tilde{\mathbf{J}}_{ext}\left(k_-,\theta,\phi,\omega\right)}{\alpha\left(k_-^2 - k_+^2\right)} \ . \tag{21}$$

From Faraday's Law (Equation A.3) an expression for the magnetic field can be derived from the above equation,

$$\begin{aligned}\hat{\mathbf{B}}(\mathbf{x},\omega) &= \frac{\mu_0}{8\pi^2 k_0^2}\int_0^{\pi/2} d\theta \sin\theta \int_0^{2\pi} d\phi \frac{k_-^2\exp\{-jk_- r|\cos\gamma|\}}{\alpha\left(k_-^2 - k_+^2\right)}\operatorname{sgn}(\cos\gamma) \\ &\times\Bigg\{\left[\left(\mathbf{\Lambda}\cdot\tilde{\mathbf{J}}_{ext}\right)_z \sin\theta\sin\phi - \left(\mathbf{\Lambda}\cdot\tilde{\mathbf{J}}_{ext}\right)_y \cos\theta\right]\mathbf{e}_x \\ &-\left[\left(\mathbf{\Lambda}\cdot\tilde{\mathbf{J}}_{ext}\right)_z \sin\theta\cos\phi - \left(\mathbf{\Lambda}\cdot\tilde{\mathbf{J}}_{ext}\right)_x \cos\theta\right]\mathbf{e}_y \\ &+\left[\left(\mathbf{\Lambda}\cdot\tilde{\mathbf{J}}_{ext}\right)_y \sin\theta\cos\phi - \left(\mathbf{\Lambda}\cdot\tilde{\mathbf{J}}_{ext}\right)_x \sin\theta\sin\phi\right]\mathbf{e}_z\Bigg\}\end{aligned} \tag{22}$$

The energy flow into the far-field is determined by the Poynting flux,

$$\mathbf{S}\left(\mathbf{x},t\right) = \frac{1}{\mu_0}\mathbf{E}\left(\mathbf{x},t\right)\times\mathbf{B}\left(\mathbf{x},t\right). \tag{23}$$

With the single Fourier mode representation of the fields the time-averaged Poynting flux becomes,

$$\left\langle\mathbf{S}\left(\mathbf{x};\omega\right)\right\rangle = \frac{1}{2\mu_0}\left\{\Re\left[\hat{\mathbf{E}}\left(\mathbf{x},\omega\right)\right]\times\Re\left[\hat{\mathbf{B}}\left(\mathbf{x},\omega\right)\right] + \Im\left[\hat{\mathbf{E}}\left(\mathbf{x},\omega\right)\right]\times\Im\left[\hat{\mathbf{B}}\left(\mathbf{x},\omega\right)\right]\right\} \ . \tag{24}$$

where $\hat{\mathbf{E}}\left(\mathbf{x},\omega\right)$ and $\hat{\mathbf{B}}\left(\mathbf{x},\omega\right)$ are given by Equations (21) and (22), respectively.

2.4 SOLUTION BY METHOD OF STATIONARY PHASE

Considering the electromagnetic field solutions only in the far-field, i.e., $k_0 r >> 1$, the method of stationary phase can be used to evaluate the integrals in Equations (21) and (22). The exponential term in the integrands can be written as,

$$\exp\left\{-jk_- r|\cos\gamma|\right\} = \exp\left\{-jk_0 r\Phi\right\} \ , \tag{25}$$

where the phase function is defined as,

$$\Phi = \tilde{k}_- |\cos\gamma|, \tag{26}$$

with $\tilde{k}_- = k_-/k_0$. When $k_0 r >> 1$ the dominant contribution to the integrals will be near the points of stationary phase (θ_s, ϕ_s) defined by the condition,

$$\left.\frac{\partial\Phi}{\partial\theta}\right|_{(\theta_s,\phi_s)} = \left.\frac{\partial\Phi}{\partial\phi}\right|_{(\theta_s,\phi_s)} = 0. \tag{27}$$

Expanding the phase function about the stationary points, the integrals in θ and ϕ can be approximated as,

$$\begin{aligned}\int_0^{\pi/2} d\theta \int_0^{2\pi} d\phi \exp\left\{-jk_-r|\cos\gamma|\right\} f(\theta,\phi) &= f(\theta_s,\phi_s)\exp\left\{-jk_0r\Phi(\theta_s,\phi_s)\right\} \\ &\times \int_0^{\pi/2} d\theta \exp\left\{-ja(\theta-\theta_s)^2\right\} \\ &\times \int_0^{2\pi} d\phi \exp\left\{-jb(\phi-\phi_s)^2\right\}\end{aligned} \tag{28}$$

where $f(\theta,\phi)$ represents the non-exponential functions in the integrands and

$$a = \left.\frac{\partial^2\Phi}{\partial\theta^2}\right|_{(\theta_s,\phi_s)}, \tag{29}$$

$$b = \left.\frac{\partial^2\Phi}{\partial\phi^2}\right|_{(\theta_s,\phi_s)}. \tag{30}$$

It can be shown that $\partial^2\Phi/\partial\theta\partial\phi = 0$ (Eqs. (41–43) below). Approximating the integrals by extending the upper limit to $+\infty$ Eq. (28) can be written,

$$\int_0^{\pi/2} d\theta \int_0^{2\pi} d\phi \exp\left\{-jk_-r|\cos\gamma|\right\} f(\theta,\phi) = \frac{\pi f(\theta_s,\phi_s)}{8k_0r|ab|^{1/2}}\left[G_1 - jG_2\right], \tag{31}$$

where,

$$G_1 = \cos(k_0r\Phi)\left[1-\mathrm{sgn}(a)\,\mathrm{sgn}(b)\right] - \sin(k_0r\Phi)\left[\mathrm{sgn}(a)+\mathrm{sgn}(b)\right] \tag{32}$$

$$G_2 = \cos(k_0r\Phi)\left[\mathrm{sgn}(a)+\mathrm{sgn}(b)\right] + \sin(k_0r\Phi)\left[1-\mathrm{sgn}(a)\,\mathrm{sgn}(b)\right] \tag{33}$$

are real functions.

With the θ and ϕ integrals in the functional form of Equation (31) the solution for the electric field [Equation (21)] can be written in terms of explicit real and imaginary components as ,

$$\begin{aligned}\hat{\mathbf{E}}(\mathbf{x},\omega) &= \frac{\omega\mu_0}{16\pi k_0^3 r}\sum_{i=1}^{N_s}\frac{k_-\sin\theta_s}{\alpha\left(k_-^2-k_+^2\right)|ab|^{1/2}} \\ &\times\left\{\left[\Re\left(\mathbf{\Lambda}\cdot\tilde{\mathbf{J}}_{ext}\right)G_1 + \Im\left(\mathbf{\Lambda}\cdot\tilde{\mathbf{J}}_{ext}\right)G_2\right]\right. \\ &\left.+j\left[-\Re\left(\mathbf{\Lambda}\cdot\tilde{\mathbf{J}}_{ext}\right)G_2 + \Im\left(\mathbf{\Lambda}\cdot\tilde{\mathbf{J}}_{ext}\right)G_1\right]\right\}\ ,\end{aligned} \tag{34}$$

where N_s is the number of stationary phase points (θ_s, ϕ_s) satisfying Equation (27) and all quantities to the right of the summation are evaluated at the stationary points. A solution for the magnetic field [Equation (22)] can be obtained in a similar manner, i.e.,

$$\begin{aligned}
\hat{B}_x(\mathbf{x},\omega) &= \frac{\mu_0}{16\pi k_0^3 r}\sum_{i=1}^{N_s}\frac{k_-^2\sin\theta_s\,\mathrm{sgn}(\cos\gamma)}{\alpha\left(k_-^2-k_+^2\right)|ab|^{1/2}} \\
&\times\Big\{\Big[\Re\left((\mathbf{\Lambda}\cdot\tilde{\mathbf{J}}_{ext})_z\sin\theta_s\sin\phi_s-(\mathbf{\Lambda}\cdot\tilde{\mathbf{J}}_{ext})_y\cos\theta_s\right)G_1 \\
&+\Im\left((\mathbf{\Lambda}\cdot\tilde{\mathbf{J}}_{ext})_z\sin\theta_s\sin\phi_s-(\mathbf{\Lambda}\cdot\tilde{\mathbf{J}}_{ext})_y\cos\theta_s\right)G_2\Big] \\
&+j\Big[-\Re\left((\mathbf{\Lambda}\cdot\tilde{\mathbf{J}}_{ext})_z\sin\theta_s\sin\phi_s-(\mathbf{\Lambda}\cdot\tilde{\mathbf{J}}_{ext})_y\cos\theta_s\right)G_2 \\
&+\Im\left((\mathbf{\Lambda}\cdot\tilde{\mathbf{J}}_{ext})_z\sin\theta_s\sin\phi_s-(\mathbf{\Lambda}\cdot\tilde{\mathbf{J}}_{ext})_y\cos\theta_s\right)G_1\Big]\Big\} \qquad (35)
\end{aligned}$$

$$\begin{aligned}
\hat{B}_y(\mathbf{x},\omega) &= -\frac{\mu_0}{16\pi k_0^3 r}\sum_{i=1}^{N_s}\frac{k_-^2\sin\theta_s\,\mathrm{sgn}(\cos\gamma)}{\alpha\left(k_-^2-k_+^2\right)|ab|^{1/2}} \\
&\times\Big\{\Big[\Re\left((\mathbf{\Lambda}\cdot\tilde{\mathbf{J}}_{ext})_z\sin\theta_s\cos\phi_s-(\mathbf{\Lambda}\cdot\tilde{\mathbf{J}}_{ext})_x\cos\theta_s\right)G_1 \\
&+\Im\left((\mathbf{\Lambda}\cdot\tilde{\mathbf{J}}_{ext})_z\sin\theta_s\cos\phi_s-(\mathbf{\Lambda}\cdot\tilde{\mathbf{J}}_{ext})_x\cos\theta_s\right)G_2\Big] \\
&+j\Big[-\Re\left((\mathbf{\Lambda}\cdot\tilde{\mathbf{J}}_{ext})_z\sin\theta_s\cos\phi_s-(\mathbf{\Lambda}\cdot\tilde{\mathbf{J}}_{ext})_x\cos\theta_s\right)G_2 \\
&+\Im\left((\mathbf{\Lambda}\cdot\tilde{\mathbf{J}}_{ext})_z\sin\theta_s\cos\phi_s-(\mathbf{\Lambda}\cdot\tilde{\mathbf{J}}_{ext})_x\cos\theta_s\right)G_1\Big]\Big\} \qquad (36)
\end{aligned}$$

$$\begin{aligned}
\hat{B}_z(\mathbf{x},\omega) &= \frac{\mu_0}{16\pi k_0^3 r}\sum_{i=1}^{N_s}\frac{k_-^2\sin\theta_s\,\mathrm{sgn}(\cos\gamma)}{\alpha\left(k_-^2-k_+^2\right)|ab|^{1/2}} \\
&\times\Big\{\Big[\Re\left((\mathbf{\Lambda}\cdot\tilde{\mathbf{J}}_{ext})_y\sin\theta_s\cos\phi_s-(\mathbf{\Lambda}\cdot\tilde{\mathbf{J}}_{ext})_x\sin\theta_s\sin\phi_s\right)G_1 \\
&+\Im\left((\mathbf{\Lambda}\cdot\tilde{\mathbf{J}}_{ext})_y\sin\theta_s\cos\phi_s-(\mathbf{\Lambda}\cdot\tilde{\mathbf{J}}_{ext})_x\sin\theta_s\sin\phi_s\right)G_2\Big] \\
&+j\Big[-\Re\left((\mathbf{\Lambda}\cdot\tilde{\mathbf{J}}_{ext})_y\sin\theta_s\cos\phi_s-(\mathbf{\Lambda}\cdot\tilde{\mathbf{J}}_{ext})_x\sin\theta_s\sin\phi_s\right)G_2 \\
&+\Im\left((\mathbf{\Lambda}\cdot\tilde{\mathbf{J}}_{ext})_y\sin\theta_s\cos\phi_s-(\mathbf{\Lambda}\cdot\tilde{\mathbf{J}}_{ext})_x\sin\theta_s\sin\phi_s\right)G_1\Big]\Big\} \qquad (37)
\end{aligned}$$

Expressions must now be found for the stationary points and second derivatives of the phase function. Recalling the definition of $\cos\gamma$ (Eq. (18)), the first derivative of Φ with respect to ϕ is,

$$\frac{\partial\Phi}{\partial\phi} = -\tilde{k}_-\,\mathrm{sgn}(\cos\gamma)\sin(\phi-\phi_{obs})\sin\theta\sin\theta_{obs}\ , \qquad (38)$$

which yields two stationary points in ϕ,

$$\phi_s = [\phi_{obs}, \pi+\phi_{obs}]\ . \qquad (39)$$

Taking the second derivative of Φ with respect to ϕ gives an expression for b,

$$b = \mp\tilde{k}_- \,\mathrm{sgn}(\cos\gamma)\sin\theta_s \sin\theta_{obs} \ , \tag{40}$$

where the -(+) root corresponds to $\phi_s = \phi_{obs}(\pi + \phi_{obs})$, respectively. It will be shown below that the latter root is the one relevant to the whistler propagation problem.

The stationary points in θ are not as easily derived but can be found from numerically solving the equation,

$$\frac{\partial\Phi}{\partial\theta} = \mathrm{sgn}(\cos\gamma)\left(\frac{\partial\tilde{k}_-}{\partial\theta}\cos\gamma + \tilde{k}_-\frac{\partial\cos\gamma}{\partial\theta}\right) = 0 \ , \tag{41}$$

where,

$$\frac{\partial\tilde{k}_-}{\partial\theta} = \frac{\tilde{k}_-\sin\theta\cos\theta}{\alpha}\left\{\bar{\epsilon}_3 - \bar{\epsilon}_1 + \frac{1}{2\tilde{k}_-^2}\left(\beta_1 - \frac{1}{\beta_2^{1/2}}\left[\beta_1^2\sin^2\theta - 2\bar{\epsilon}_2^2\bar{\epsilon}_3^2\right]\right)\right\} \tag{42}$$

$$\frac{\partial\cos\gamma}{\partial\theta} = \cos\theta\sin\theta_{obs}\cos(\phi_s - \phi_{obs}) - \sin\theta\cos\theta_{obs} \ , \tag{43}$$

with,

$$\beta_1 = \bar{\epsilon}_1^2 - \bar{\epsilon}_2^2 - \bar{\epsilon}_1\bar{\epsilon}_3 \ , \tag{44}$$

$$\beta_2 = \beta_1^2\sin^4\theta + 4\bar{\epsilon}_2^2\bar{\epsilon}_3^2\cos^2\theta \ . \tag{45}$$

and the $\mathrm{sgn}(\cos\gamma)$ factor can be dropped when determining the roots. Differentiating Eq. (41) with respect to θ yields the following expression for the a coefficient,

$$a = \mathrm{sgn}(\cos\gamma)\left(\frac{\partial^2\tilde{k}_-}{\partial\theta^2}\cos\gamma + 2\frac{\partial\tilde{k}_-}{\partial\theta}\frac{\partial\cos\gamma}{\partial\theta} + \tilde{k}_-\frac{\partial^2\cos\gamma}{\partial\theta^2}\right) \tag{46}$$

where,

$$\begin{aligned}\frac{\partial^2\tilde{k}_-}{\partial\theta^2} &= \frac{1}{\tilde{k}_-}\left(\frac{\partial\tilde{k}_-}{\partial\theta}\right)^2 + \frac{\sin^2\theta\cos^2\theta}{\alpha\tilde{k}_-\beta_2^{1/2}}\left(\frac{\beta_3^2}{\beta_2} - \beta_1^2\right) \\ &\quad + \frac{\partial\tilde{k}_-}{\partial\theta}\left[\frac{2\sin\theta\cos\theta(\bar{\epsilon}_3 - \bar{\epsilon}_1)}{\alpha} + \frac{\cos^2\theta - \sin^2\theta}{\cos\theta\sin\theta} - \frac{\sin\theta\cos\theta}{\alpha\tilde{k}_-^2}\left(\beta_1 - \frac{\beta_3}{\beta_2^{1/2}}\right)\right]\end{aligned} \tag{47}$$

$$\frac{\partial^2\cos\gamma}{\partial\theta^2} = -\cos\gamma \ , \tag{48}$$

with,

$$\beta_3 = \beta_1^2\sin^2\theta - 2\bar{\epsilon}_2^2\bar{\epsilon}_3^2 \ . \tag{49}$$

In the whistler regime the resonance angle θ_{res} satisfies Eq. (A.42),

$$\tan^2\theta_{res} = \left|\frac{\bar{\epsilon}_e}{\bar{\epsilon}_1}\right| . \tag{50}$$

When θ approaches the resonance angle then $\alpha(\theta) \to 0$ and the wave vector $k_- \to \infty$ (Eq.(12)) so that to lowest order the stationary phase condition (Eq. 27) goes as,

$$\frac{\partial \Phi}{\partial \theta} \to \text{Constant} \frac{|\cos\gamma|}{\alpha^2}, \tag{51}$$

where the constant contains dielectric tensor components and trigonometric functions of θ. For the stationary point to be defined it must be true that,

$$|\cos\gamma| \to 0, \tag{52}$$

or,

$$\tan\theta_{obs} \to -\frac{1}{\tan\theta_s \cos\left(\phi_s - \phi_{obs}\right)}. \tag{53}$$

For $0 \le \theta_{obs} \le \pi/2$ and $0 \le \theta_s \le \pi/2$ this limit exists only if $\phi_s - \phi_{obs} = \pi$, i.e., the second root in Eq. (39). Furthermore, precisely at resonance,

$$\theta_{obsRes} = \pi/2 - \theta_{res}. \tag{54}$$

Note that if (θ_{obs}, θ_s) is a solution to the θ_s stationary point equation (Eq. 41) then $(\theta'_{obs}, \theta'_s)$ is also a solution when $\theta'_{obs} = \pi/2 - \theta_{obs}$ and $\theta'_s = \pi/2 - \theta_s$. Thus the same condition on ϕ_s exists when $\pi/2 \le \theta_{obs} \le \pi$.

In summary, stationary points are found by setting $\phi_s - \phi_{obs} = \pi$ and then solving Eq. (41) for θ_s in the range $0 \le \theta_s \le \pi/2$. This solution can be used for $0 \le \theta_{obs} \le \pi/2$ and for $\pi/2 \le \theta_{obs} \le \pi$ using the θ'_{obs} and θ'_s definitions given above.

2.5 TREATMENT NEAR RESONANCE

As θ_{obs} approaches its resonance value the electric and magnetic field solutions become singular and the collisionless linear theory breaks down. There are a number of physical mechanisms which might come into play with large wave field amplitudes, e.g., particle trapping and pump-wave driven plasma turbulence. It is beyond the scope of this report to develop models for or to speculate on the relevant non-linear effects—indeed, the main objective of the DSX mission is to gather the data necessary to guide such model development and validation. Instead, a limiting value of θ_{obs} is sought which can be used to evaluate the electric and magnetic field expressions and is defined consistently within the context of the linear theory. This is done by considering the effect of a finite collision frequency.

For a stationary ion plasma with dielectric components defined by Eqs. (A.26)-(A.28), the right-hand side of the resonance relation (Eq. A.42) can be expanded to lowest order in the normalized collision frequency Z_e as,

$$\tan^2\theta = -\frac{\bar{\epsilon}_3}{\bar{\epsilon}_1}\left(1 - j g_1 Z_e\right) \ , \tag{55}$$

where,

$$g_1 = \frac{1-\bar{\epsilon}_3}{\bar{\epsilon}_3} - \frac{1-\bar{\epsilon}_1}{\bar{\epsilon}_1}\left(\frac{1+Y^2}{1-Y^2}\right) \ , \tag{56}$$

and the $\bar{\epsilon}$'s are the dielectric components in the $Z_e = 0$ limit. The following question is posed: What is the differential angle $\delta\theta = \theta - \theta_{res}$ at which the deviation in magnitude of $\tan^2\theta$ about $\tan^2\theta_{res}$ is of the order of the magnitude of the collision term? This difference in angle will then be taken to be the closest θ can be to θ_{res} before the collisionless linear theory breaks down. Using Eq. 55, the defining relation for $\delta\theta$ is,

$$\left|\tan^2(\theta_{res} - \delta\theta) - \tan^2\theta_{res}\right| = \left|g_1 Z_e \frac{\bar{\epsilon}_3}{\bar{\epsilon}_1}\right| \ . \tag{57}$$

With $\delta\theta << \theta_{res}$ the left hand side can be expanded to yield,

$$\delta\theta \sim \left|\frac{\cos^3\theta_{res}}{2\sin\theta_{res}} g_1 Z_e \frac{\bar{\epsilon}_3}{\bar{\epsilon}_1}\right| = \frac{1}{2}\cos\theta_{res}\sin\theta_{res}\left|g_1 Z_e\right| \ . \tag{58}$$

The closest observational angle to resonance to use in the computations, θ_{obs0} is then estimated as,

$$\theta_{obs0} = \pi/2 - \theta_{res} - \delta\theta \ . \tag{59}$$

It should be emphasized that this approach to the treating angles close to resonance is by no means rigorous, either in a physical or mathematical sense. Rather, it is an ad-hoc estimate that can be used to consistently impose a limiting angle for electric and magnetic field calculations within the stationary phase approximation. It is expected to be supplanted by a much better non-linear model motivated by empirical results from DSX.

3. ANTENNA IMPEDANCE FUNCTION

The electric and magnetic field amplitudes depend on a specified current amplitude I_0 at the dipole feeds. For the case of of specific DSX experiments, these can be obtained directly from current measurements. Alternatively, values for I_0 can be estimated as a function of the driving voltage V_0 from an appropriate impedance model using the generalized Ohm's law, i.e.,

$$V_0 = I_0 Z_{dipole} \tag{60}$$

where Z_{dipole} is the input impedance of the dipole antenna. Since only the relative phases are meaningful, the phase is chosen so that the phase of I_0 is 0 for the work presented in this report.

The impedance function implemented will be that derived by Balmain [11] for a thin monopole of length $d/2$ and radius r_{ant} ($r_{ant} << d/2$) in a cold, magnetized and stationary ion plasma. From Equation (62) in his paper,

$$Z_{mono} = \frac{a}{j\omega\pi\epsilon_0\bar{\epsilon}_1 dF^{1/2}}\left[\ln\left(\frac{dF}{r_{ant}(a+F^{1/2})}\right) - 1\right] \tag{61}$$

where,

$$F = \sin^2\beta_{ant} + a^2\cos^2\beta_{ant} \tag{62}$$

$$a^2 = \frac{\bar{\epsilon}_1}{\bar{\epsilon}_3} \tag{63}$$

Balmain's original notation has been switched to be consistent with that used in this report. In particular (Balmain notation on the right-hand side),

$$\begin{aligned}
\bar{\epsilon_1} &= K' \quad \text{(dielectric constants)} \\
\bar{\epsilon_3} &= K_0 \\
d &= 2L \quad \text{(dipole antenna length)} \\
r_{ant} &= \rho \quad \text{(antenna radius)} \\
\beta_{ant} &= \theta \quad \text{(antenna orientation angle)}
\end{aligned}$$

For a dipole antenna the impedance is twice that of the monopole, $Z_{dipole} = 2Z_{mono}$. The impedance was derived by estimating the power dissipated at the surface of the antenna (Equation 54 in [11]) using an expression for the electric field derived from a scalar potential (Equation 46 in [11]). There is some degree of low frequency approximation made—the full expression for the electric field (Equation 4 in [11]) has a term proportional to the frequency and vector potential which is being neglected. No estimate has been made of the consequences of this omission.

In the whistler regime, the a^2 factor (Eq. 63) is negative and there is a critical antenna orientation angle β_{crit} at which $F = 0$ and Z_{in} becomes singular. From Eqs. (62) and (A.42) it can be seen that the critical orientation angle and resonance angle are related through a^2,

$$\tan^2\beta_{crit} = \left|a^2\right| = \frac{1}{\tan^2\theta_{res}}, \tag{64}$$

which indicates,

$$\beta_{crit} = \pi/2 - \theta_{res} \ . \tag{65}$$

When evaluating $a = (a^2)^{1/2} = \pm j|a|$ it is emphasized that the plus root is taken to be consistent with causal propagation in the whistler regime. For $\beta_{ant} < \beta_{crit}$, $F < 0$ and $F^{1/2} = \pm j|F|^{1/2}$. To be consistent with the convention for a,when $\beta_{ant} \to 0$ the plus root should be taken.

Expressing the dipole impedance in terms of a real resistance component R and an imaginary reactance component χ,

$$Z_{dipole} = R + j\chi \ , \tag{66}$$

Eq. 61 can be expanded out for $0 \leq \beta_{ant} < \beta_{crit}$ to yield,

$$R = 2\frac{|a|}{\omega\pi\epsilon_0\bar{\epsilon}_1 d|F|^{1/2}}\frac{\pi}{2} \ , \tag{67}$$

$$\chi = -2\frac{|a|}{\omega\pi\epsilon_0\bar{\epsilon}_1 d|F|^{1/2}}\left[\ln\left(\frac{d|F|}{r_{ant}(|a| + |F|^{1/2})}\right) - 1\right] \ , \tag{68}$$

and for $\beta_{crit} < \beta_{ant} \leq \pi/2$ the components become,

$$R = 2\frac{|a|}{\omega\pi\epsilon_0\bar{\epsilon}_1 d|F|^{1/2}}\left[\ln\left(\frac{d|F|}{r_{ant}(|a^2| + |F|)^{1/2}}\right) - 1\right] \ , \tag{69}$$

$$\chi = -2\frac{|a|}{\omega\pi\epsilon_0\bar{\epsilon}_1 d|F|^{1/2}}\xi \ , \tag{70}$$

where,

$$\tan\xi = \frac{|a|}{|F|^{1/2}} \ . \tag{71}$$

The Balmain impedance formulas must be approached with caution as they contain some singular behavior, e.g., the resistance and reactance both go to infinity at the critical orientation angle. Furthermore, in regions close to β_{crit} the resistance can become negative and the reactance positive. Understanding the limits of the Balmain approach and improving the impedance estimates are a major objective of the DSX mission. For the baseline analysis in this report, the Balmain impedances will be used as given above and their potential limitations should be kept in mind.

To illustrate the behavior of the Balmain impedance, a specific case is considered relevant to DSX deep in the plasmasphere at the magnetic equator. In particular, let $n_e = 1.62 \times 10^3$ cm^{-3} and $B_0 = 3.50 \times 10^{-2}$ G - values corresponding to an L-shell $L = 2.1$ and magnetic latitude $MLat = -0.06^\circ$ consistent with the orbit shown in Figure 2. The Y-boom antenna dimensions are taken to be $d = 80$m and r_{ant} the effective radius of the equilateral boom, i.e., $r_{ant} = a_{eff} = 1.15 \times 10^{-1}$ m (Section 2.1). In Figure 5 the reactance (top) and resistance (bottom) computed from Eqs. (67)–(70) are shown as functions of frequency for $\beta_{ant} = 0^\circ$ and 90°. Also shown are the values for an equivalent size dipole $in - vaccuo$ as computed from the following formulas [15],

$$R_{vac} = 80\pi^2\left(\frac{d}{\lambda_0}\right)^2 \ , \tag{72}$$

$$\chi_{vac} = 120\frac{\log\left(\frac{d}{2r_{ant}}\right) - 1}{\tan\left(\frac{k_0 d}{2}\right)} \ . \tag{73}$$

where $\lambda_0 = 2\pi/k_0$.

Figure 6 shows the impedances as a function of β_{ant} at frequencies of 3, 10 and 30 kHz with an x-axis resolution of 0.5°. The singular nature of the impedance function is obvious as the antenna orientation angle sweeps through the critical angle, $\beta_{crit} = 1.23°$, 5.92° and 18.39° for 3 kHz, 10 kHz and 30 kHz, respectively. Near the critical angle anomalous behavior of R and χ can be seen, for example, in the gap in R near 6° where negative values were encountered and not plotted and the sudden dip in the -χ. There is a significant difference in behavior for antenna orientation angles above and below the critical orientation angle where the functional forms of the impedances switch—a result of F^2 going from negative to positive and the leading factor in Eq. (61) going from imaginary to real. Reactances in the plasma are smaller than $in - vacuuo$ indicating larger antenna capacitances. The plasma resistances are significantly higher than those in a vacuum. Within the collisionless cold-plasma formulation, there is no heating or energy propagation due to plasma motion (Chapter 4, [16]) and consequently the resistance represents energy carried away by the Poynting flux. The Balmain resistance can be compared to radiation resistances computed from appropriate spatial averages of the stationary phase solution for the Poynting flux (Eq. 24). More will be said about this in Section 4.

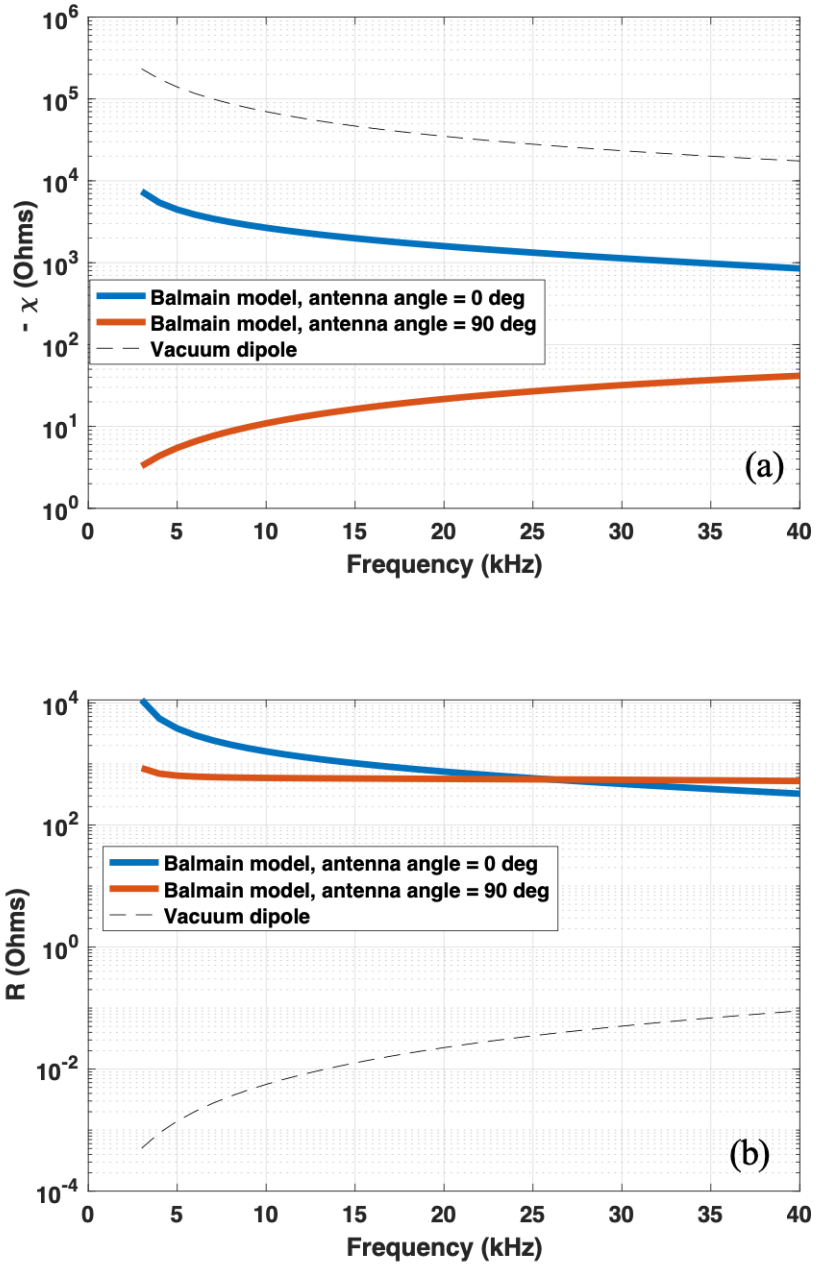

Figure 5. The Balmain reactance (a) and resistance (b) for a model of the DSX Y-boom antenna deep in the magnetosphere at the magnetic equator (see text for the nominal DSX plasma parameters) as function of frequency for antenna orientation angles of $\beta_{ant} = 0°$ and $90°$. The values for an equivalent size antenna in a vacuum are shown as dashed lines.

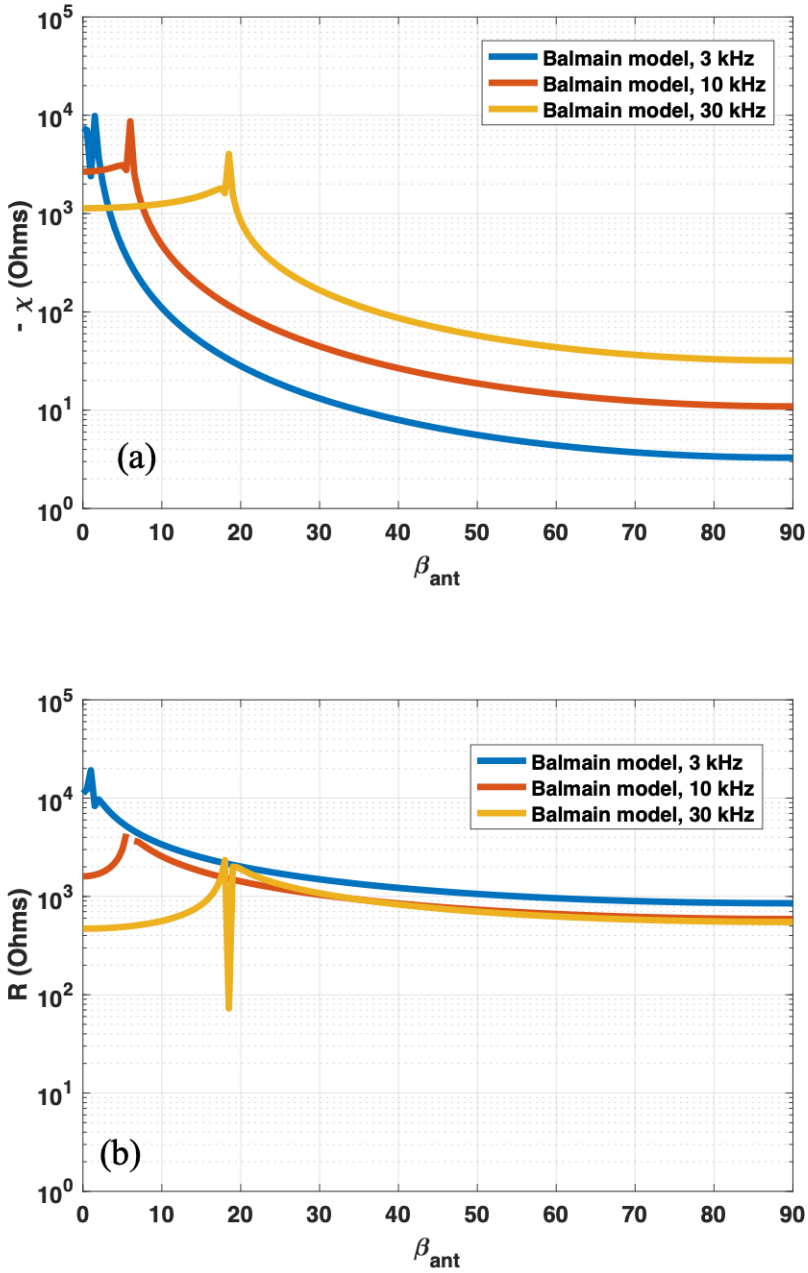

Figure 6. The Balmain reactance (a) and resistance (b) for a model of the DSX Y-boom antenna and nominal plasma parameters as function of antenna orientation angles β_{ant} for fixed frequencies of 3 kHz, 10 kHz and 30 kHz.

This page intentionally left blank.

4. RESULTS

Algorithms to compute the stationary phase solutions for the electric and magnetic fields have been implemented in a MATLAB code. In this section examples for the nominal parameter set defined in Section 3, i.e., DSX inside the plasmasphere at the magnetic equator will be presented. The intent is to illustrate some features of a VLF emitter in the magnetosphere, not to present a comprehensive survey of the DSX parameter regime or to explore what the parameters might be for a system optimized to produce far-field radiation. In addition to the density and magnetic field, an electron temperature must be specified in order to compute the collision term Z_e (Eq. A.25) used to estimate the limiting observational angle θ_{obs0} (Eq. 59). Referencing the model of Kutiev, et al. [17] based on Akebono satellite data, this value is taken to be $T_e = 7.10 \times 10^3$ for the nominal DSX parameter set. The far-field solutions were computed at a distance $r_{obs} = 200$ km.

The magnitude of the k vectors for the propagating whistler modes, i.e., k_- (Eq. (12)), are shown as a function of θ_{obs} in Figure 7 for the frequencies 3 kHz, 10 kHz and 30 kHz. Vacuum values k_0 are also shown. The divergence as $\theta_{obs} \to \theta_{obsRes}$ is apparent with the value of θ_{obsRes} increasing with increasing frequency. Wavelengths in the plasma are shorter than those in vacuum for all θ_{obs} and go to zero as resonance is approached.

Figures 8 and 9 show the electric field and magnetic field solutions, respectively, at 10 kHz as functions of θ_{obs} for antenna orientation angles of $\beta_{ant} = 0^\circ$ (red) and 90° (blue). The ϕ_{obs} angle is fixed at $\phi_{obs} = 0^\circ$. The curves shown in frames (b) are the same as shown in frames (a), but with the x-axis zoomed-in to the region close to the resonance angle. Vertical dotted lines indicate the values $\theta_{obs} = \theta_{obs0}$ (Eq. 59) and a value $\theta_{obs} = \theta_{obs1}$ chosen just prior to the θ_{obs} value where the $\beta_{ant} = 90^\circ$ starts to oscillate in θ_{obs}. This oscillation might well be a relic of the stationary phase approximation. In the discussion that follows the region between θ_{obs1} and θ_{obs0} will be referred to as the "resonance region."

In Figure 10 the behavior of the electric field (top panel) and magnetic field (bottom panel) as functions of ϕ_{obs} are illustrated. Values for the fields are plotted at the specific angles $\theta_{obs} = \theta_{obs0}$ and θ_{obs1} as described above, and for the antenna orientation angles of $\beta_{ant} = 0^\circ$ and 90°. For $\beta_{ant} = 0$ the fields are uniform in ϕ_{obs}, as expected, but exhibit large variations in amplitude and oscillatory behavior when $\beta_{ant} = 90^\circ$. It is suspected that the oscillations are an effect of the stationary phase approximation, but the the envelope of maximum angles might be a realistic approximation to the physical amplitudes. There is a huge difference in amplitudes between the curves at the two different θ_{obs} values shown for both antenna orientation angles, indicating that most of the power is being transmitted in the resonance region cone.

The focusing of radiated power in the resonance region is illustrated in Figure 11 where the radial Poynting flux, S_r (Eq. 24), normalized to I_0^2 averaged over ϕ_{obs} in the upper-hemisphere is shown as a function of θ_{obs} at 10 kHz and for $\beta_{ant} = 0^\circ$ and 90°. Figure 12 shows the corresponding radiation patterns represented as an intensity plot of the normalized S_r on the unit sphere. Both the asymmetry in ϕ_{obs} when $\beta_{ant} \neq 0$ and the concentration in power in the resonance region can be seen.

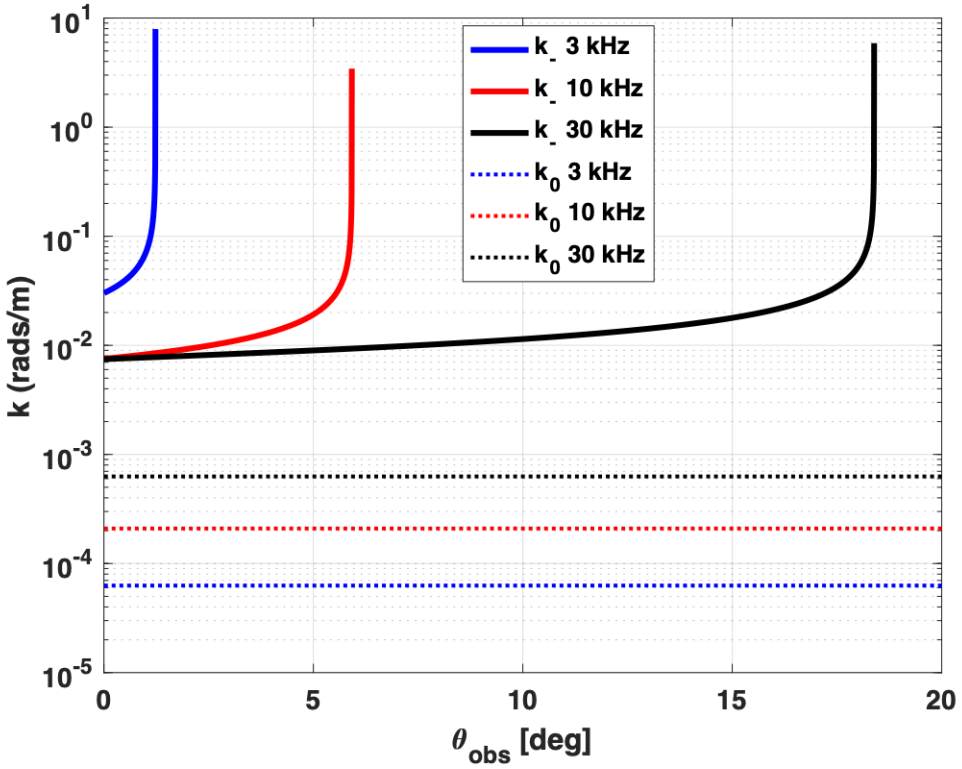

Figure 7. The magnitude of the propagating k vector (k_{-}) as a function of the observational angle with respect to the background magnetic field (θ_{obs}) for the nominal DSX parameter set at 3 kHz, 10 kHz and 30 kHz. The vacuum values k_0 are shown as dotted lines.

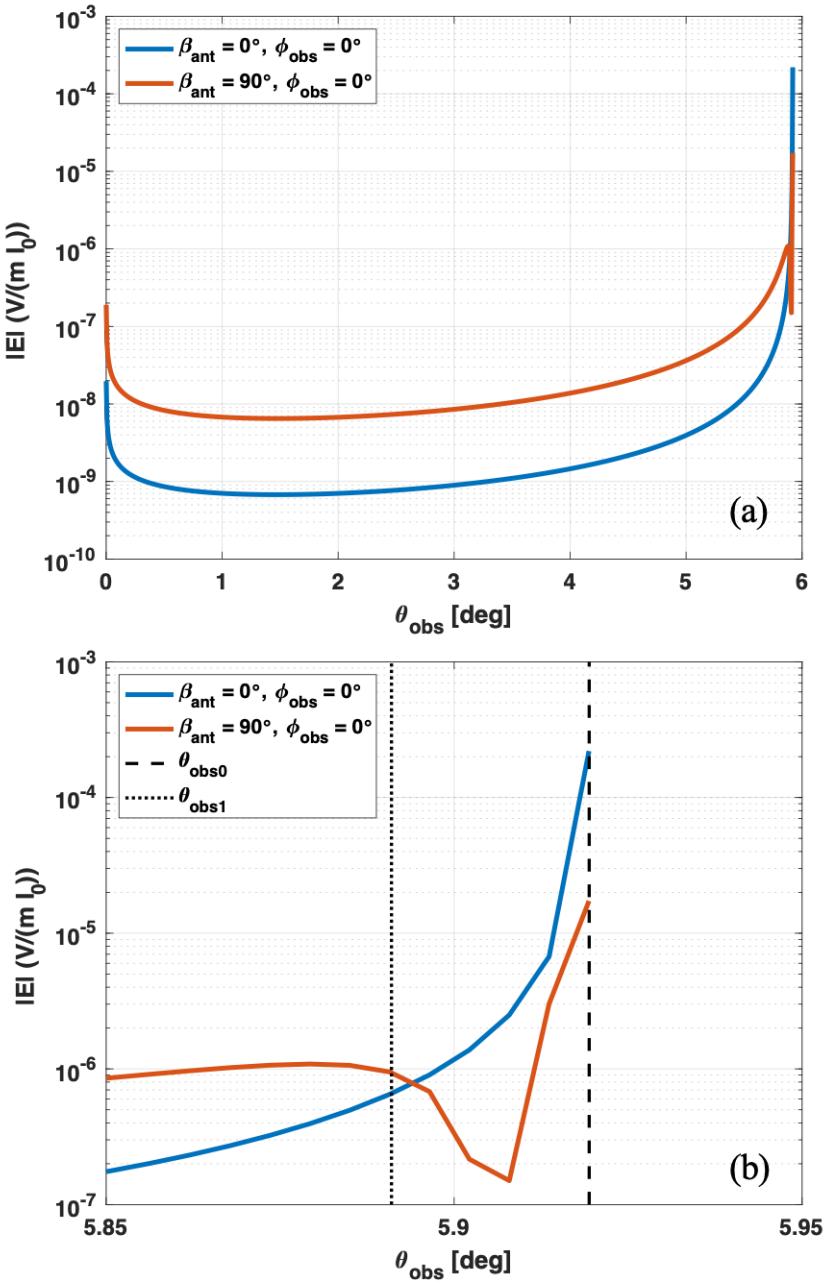

Figure 8. The magnitude of the electric field $|\mathbf{E}|$ as a function of θ_{obs} at 10 kHz for the nominal DSX parameter set. The bottom panel is the same as the top panel but at higher resolution in θ_{obs} region near the resonance region.

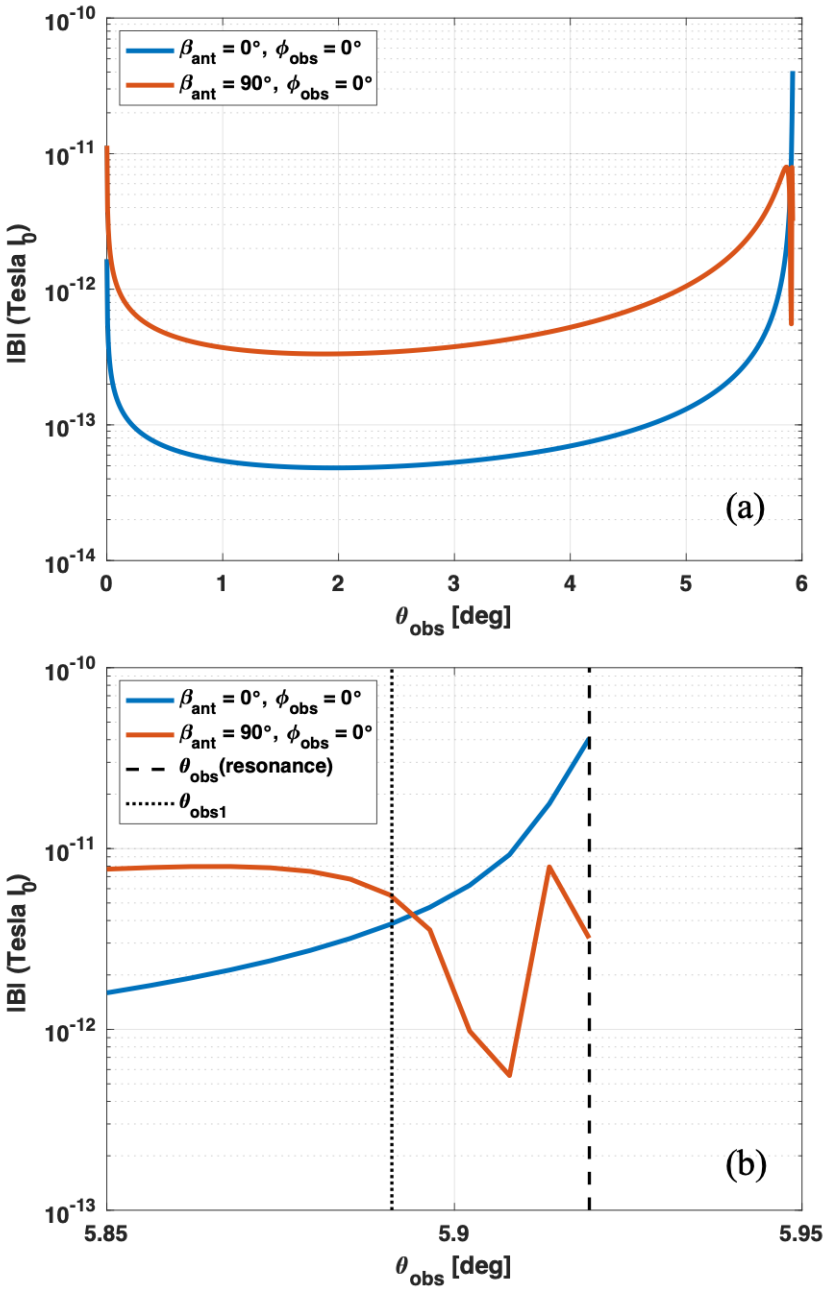

Figure 9. The magnitude of the magnetic field $|\mathbf{B}|$ as a function of θ_{obs} at 10 kHz for the nominal DSX parameter set. The bottom panel is the same as the top panel but at higher resolution in θ_{obs} region near the resonance region.

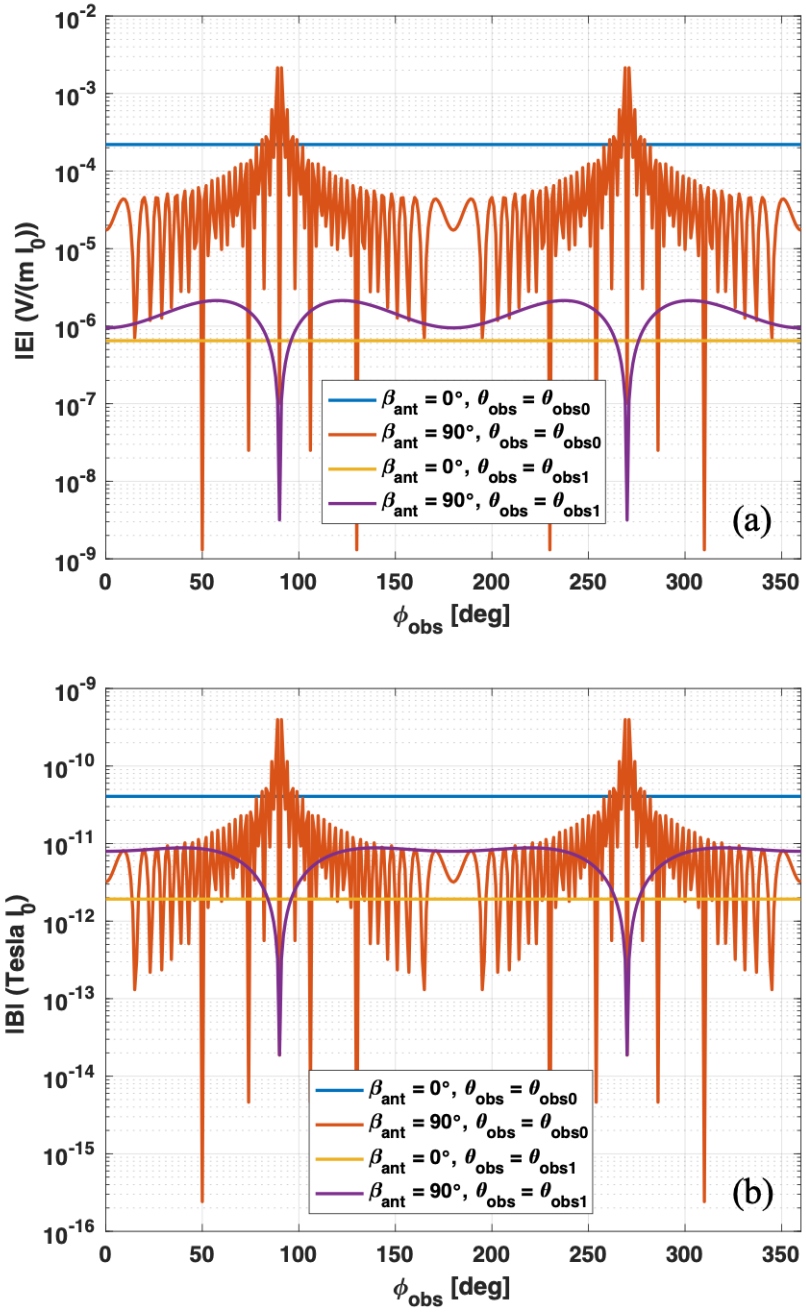

Figure 10. The magnitude of the electric field $|\mathbf{E}|$ *(a) and magnetic field* $|\mathbf{B}|$ *(b) as a function of* ϕ_{obs} *at 10 kHz for* $\beta_{ant} = 0°$ *and* $90°$*. Values at the* θ_{obs0} *and* θ_{obs1} *bounding the resonance regions are shown.*

Integrating the normalized Poynting flux over the full sphere (twice the value of integrating over the upper hemisphere) at $r = r_{obs}$ yields values for the total radiated power. The total radiated power normalized to I_0^2 is equivalent to the far-field radiation resistance R_{rad}. Figure 13 shows the total normalized power for the nominal DSX parameter set at 10 kHz as a function of the antenna orientation angle for both S_r integrated only to θ_{obs1} and for S_r integrated all the way through the resonance region to θ_{obs0}. Also shown is the radiation resistance for the equivalent dipole $in-vacuuo$. Comparing the plasma curves it is clear that all of the power is being radiated in the resonance region. Notwithstanding the jumpy behavior in β_{ant} near and before β_{crit}, the qualitative behavior of the power integrated through the resonance regime is similar to the Balmain resistance (Figure 6). Quantitatively, however, they are several orders of magnitude apart!

Finally, the Balmain impedance relation can be used to estimate I_0 for a transmitter driving voltage of $V_0 = 5$ kV by using Ohms' Law (Eq. 60),

$$|I_{0|} = \frac{|V_0|}{|Z_{dipole}|}, \tag{74}$$

where Z_{dip} is given by Eqs. (66)–(70). Applying these values to normalized total power curves in Figure 13, absolute power estimates are obtained as shown in Figure 14. Though the radiation resistances are larger for smaller antenna orientation angles, the combined effect of Ohm's law and the stationary phase solutions indicate that for a fixed voltage more power is radiated into the plasma when the antenna is oriented orthogonal to the magnetic field.

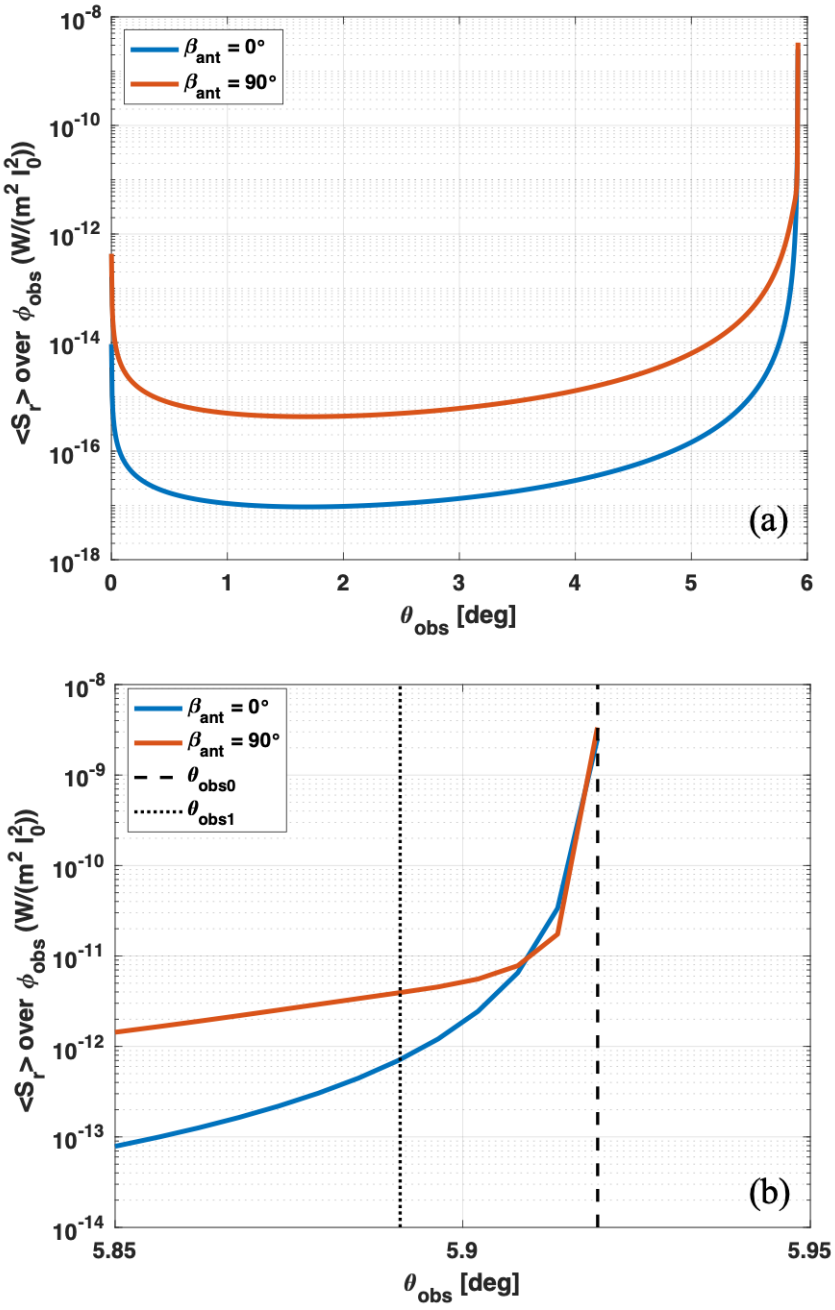

Figure 11. The radial Poynting flux $< S_r >$ at 10 kHz averaged over ϕ_{obs} in the upper hemisphere and normalized to I_0^2 as a function of θ_{obs} for $\beta_{ant} = 0°$ and 90°, and the nominal DSX parameter set. The curves shown in frames (b) are the same as shown in frames (a), but with the x-axis zoomed-in to the region close to the resonance angle.

.

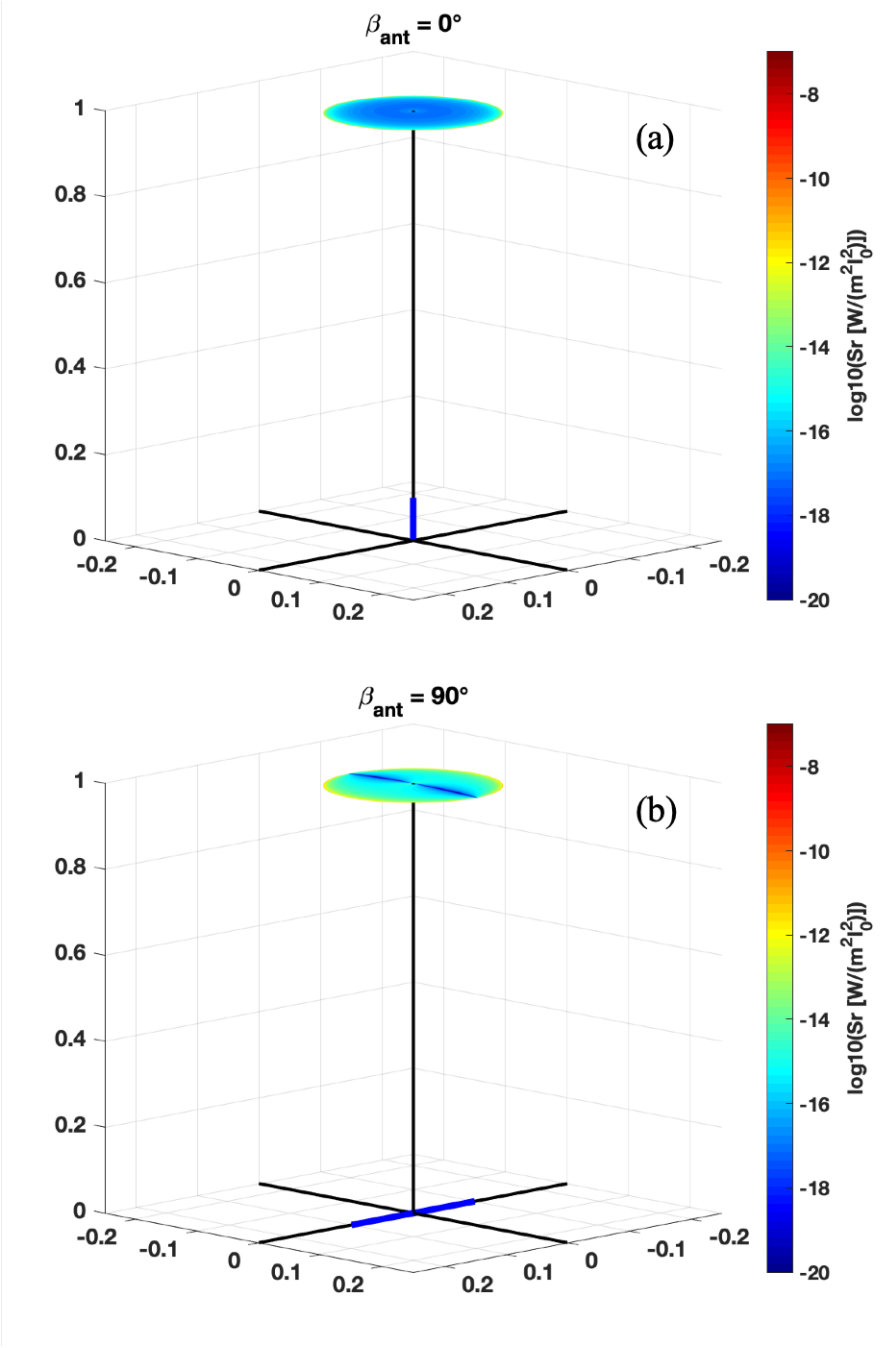

Figure 12. The intensity of the radial Poynting flux S_r at 10 kHz normalized to $|^2_0$ shown on a unit sphere in the upper hemisphere for $\beta_{ant} = 0°$ (a) and 90° (b), and the nominal DSX parameter set.

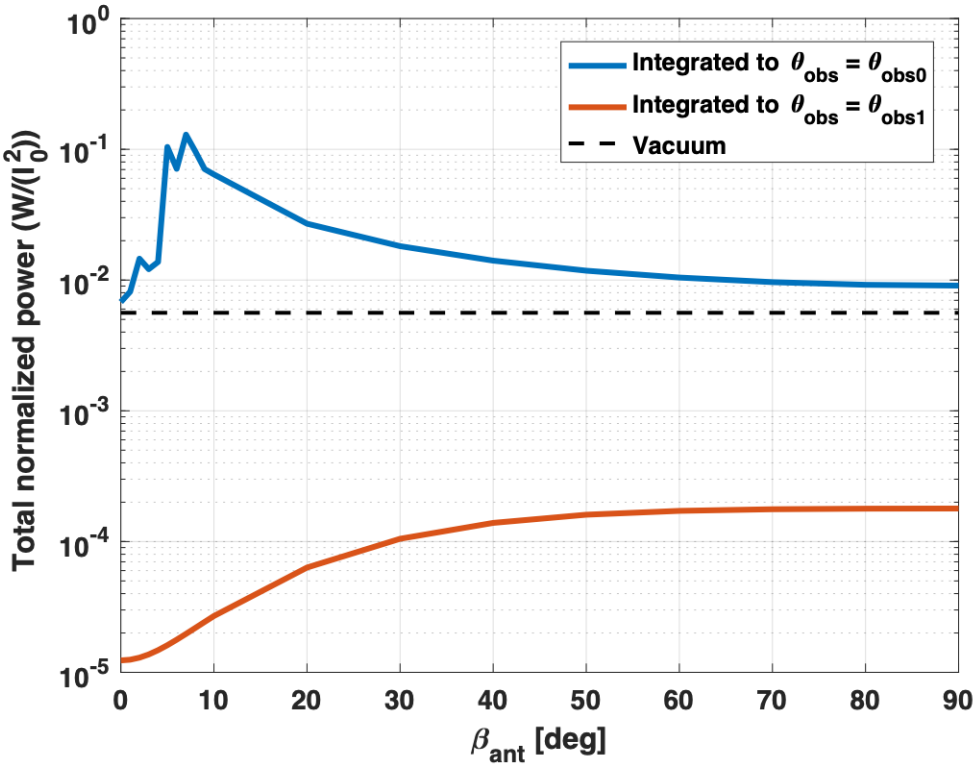

Figure 13. The total normalized power at 10 kHz as a function of antenna orientation angle β_{ant} for the Poynting flux integrated to θ_{obs1} just before the resonance region (brown) and integrated to θ_{obs0} through the resonance region. The nominal DSX parameter set is used. Vacuum values are shown as a dotted line.

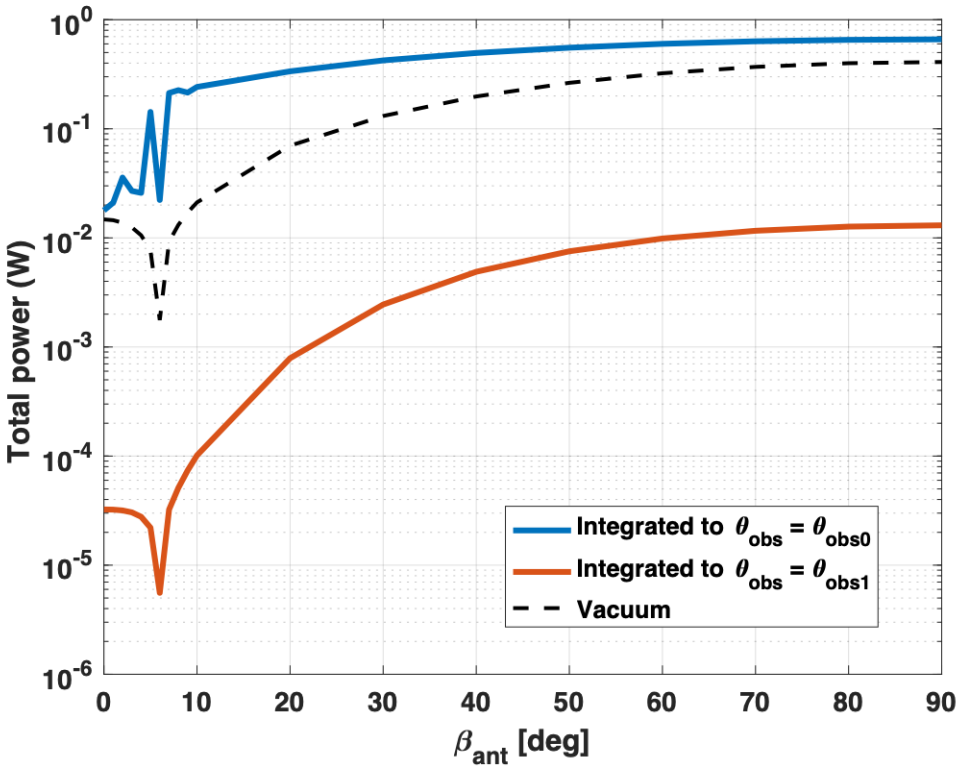

Figure 14. The total absolute power using I_0 estimated from the Balmain impedance for a driving voltage of 5 kV as a function of antenna orientation angle β_{ant} for the Poynting flux integrated to θ_{obs1} just before the resonance region (brown) and integrated to θ_{obs0} to include the resonance region. The nominal DSX parameter set is used. Vacuum values are shown as a dotted line.

APPENDIX A: COLD PLASMA BASICS

Fundamental to the analysis are Maxwell's equations,

$$\nabla \cdot \mathbf{E} = \frac{\rho}{\epsilon_0} , \tag{A.1}$$

$$\nabla \times \mathbf{B} = \mu_0 \mathbf{J} + \frac{1}{c^2} \frac{\partial \mathbf{E}}{\partial t} , \tag{A.2}$$

$$\nabla \times \mathbf{E} = -\frac{\partial \mathbf{B}}{\partial t} , \tag{A.3}$$

$$\nabla \cdot \mathbf{B} = 0 . \tag{A.4}$$

where $\mathbf{E}(\mathbf{x}, t)$ is the electric field, $\mathbf{B}(\mathbf{x}, t)$ is the magnetic fild, ρ is the charge density, $\mathbf{J}$ is the current density, ϵ_0 is the permittivity of free-space, $\mu_0 = 1/\epsilon_0 c^2$ is the magnetic vacuum permeability and c is the speed of light. In a plasma with N particle species the current and charge densities are given in terms of the species i number density n_i, charge q_i and average velocity $\mathbf{v}_i$ as,

$$\rho = \sum_{j=1}^{N} n_i q_i , \tag{A.5}$$

$$\mathbf{J} = \sum_{j=1}^{N} n_i q_i \mathbf{v}_i , \tag{A.6}$$

and are related by the equation of charge continuity,

$$\frac{\partial \rho}{\partial t} + \nabla \cdot \mathbf{J} = 0 . \tag{A.7}$$

The equation of motion for each species is given by,

$$\frac{d\mathbf{p}}{dt} = q_i \left(\mathbf{E} + \mathbf{v}_i \times \mathbf{B} \right) - \nu_i \mathbf{v}_i, \tag{A.8}$$

where $\mathbf{p}_i = \gamma m_i \mathbf{v}_i$ is the particle momentum, $\gamma = \left[1 + (pc/mc^2)^2\right]^{1/2}$ is the relativistic factor, ν_i is the effective collision frequency, and c is the speed of light.

In the linear response limit a magnetic field of the form $\mathbf{B} = \delta\mathbf{B} + B_0 \mathbf{e}_z$, where $B_0 >> \delta\mathbf{B}$ and $(\delta\mathbf{B}, \mathbf{E}, \mathbf{v})$ are all considered first-order. The current density can be expressed as,

$$\mathbf{J} = \mathbf{J}_{int} + \mathbf{J}_{ext} \tag{A.9}$$

where $\mathbf{J_{ext}}$ is an applied external current and $\mathbf{J_{int}}$ is the self-consistent first-order solution for the internal plasma current density. Representing all the dynamic variables as Fourier modes in both space and time (e.g., Eqs. 1-2) the following non-relativistic wave equation can be derived from Eqs. A.1-A.9 (e.g., [16]),

$$\left(\mathbf{kk} - k^2 \mathbf{I} + \omega^2 \mu_0 \boldsymbol{\epsilon} \right) \cdot \tilde{\mathbf{E}} = j\omega\mu_0 \tilde{\mathbf{J}}_{ext} . \tag{A.10}$$

where,

$$\boldsymbol{\epsilon} = \epsilon_0 \begin{bmatrix} \bar{\epsilon}_1 & j\bar{\epsilon}_2 & 0 \\ -j\bar{\epsilon}_2 & \bar{\epsilon}_1 & 0 \\ 0 & 0 & \bar{\epsilon}_3 \end{bmatrix} \tag{A.11}$$

The tensor components are defined as,

$$\bar{\epsilon}_1 = 1 - \frac{\omega_{pe}^2 U_e}{\omega^2 U_e^2 - \omega_{ce}^2} - \sum_{i=1}^{N_{ion}} \frac{\omega_{pi}^2 U_i}{\omega^2 U_i^2 - \omega_{ci}^2} \tag{A.12}$$

$$\bar{\epsilon}_2 = -\frac{\omega_{pe}^2 \omega_{ce}}{\omega\left(\omega^2 U_e^2 - \omega_{ce}^2\right)} + \sum_{i=1}^{N_{ion}} \frac{\omega_{pi}^2 \omega_{ci}}{\omega\left(\omega^2 U_i^2 - \omega_{ci}^2\right)} \tag{A.13}$$

$$\bar{\epsilon}_3 = 1 - \frac{\omega_{pe}^2}{U_e \omega^2} - \sum_{i=1}^{N_{ion}} \frac{\omega_{pi}^2}{U_i \omega^2} \tag{A.14}$$

where,

$$\omega_{ce(i)} = \frac{|q_{e(i)}| B_0}{m_{e(i)}} \tag{A.15}$$

$$\omega_{pe(i)} = \left(\frac{n_{e(i)} q_{e(i)}^2}{m_{e(i)} \epsilon_0}\right)^{1/2} \tag{A.16}$$

$$U_{e(i)} = 1 - j\frac{\nu_{e(i)}}{\omega} \tag{A.17}$$

and N_{ion} is the number of ion species.

Another popular representation of the dielectric tensor components is,

$$\bar{\epsilon}_1 = S = \frac{1}{2}(R + L) \tag{A.18}$$

$$\bar{\epsilon}_2 = D = \frac{1}{2}(R - L) \tag{A.19}$$

$$\bar{\epsilon}_3 = P \tag{A.20}$$

where,

$$R = 1 - \frac{\omega_{pe}^2}{\omega(\omega U_e - \omega_{ce})} - \frac{\omega_{pi}^2}{\omega(\omega U_i + \omega_{ci})} \tag{A.21}$$

$$L = 1 - \frac{\omega_{pe}^2}{\omega(\omega U_e + \omega_{ce})} - \frac{\omega_{pi}^2}{\omega(\omega U_i - \omega_{ci})} \tag{A.22}$$

For a two-component electron and single ion plasma the X, Y, Z notation is often used where,

$$X = \frac{\omega_{pe}^2 + \omega_{pi}^2}{\omega^2}\,, \tag{A.23}$$

$$Y = \frac{\omega_{ce}}{\omega}\,, \tag{A.24}$$

$$Z_{e(i)} = \frac{\nu_{e(i)}}{\omega}. \tag{A.25}$$

Letting $\alpha_m = m_i/m_e$ be the ion-to-electron mass ratio the dielectric tensor elements can be written as,

$$\bar{\epsilon}_1 = 1 - \frac{X}{(1+\alpha^{-1})} \frac{1 - jZ_e}{\left((1-jZ_e)^2 - Y^2\right)} - \frac{X}{(1+\alpha)} \frac{1 - jZ_i}{\left((1-jZ_i)^2 - \alpha^{-2}Y^2\right)} \tag{A.26}$$

$$\bar{\epsilon}_2 = -\frac{X}{(1+\alpha^{-1})} \frac{Y}{\left((1-jZ_e)^2 - Y^2\right)} + \frac{X}{(1+\alpha)} \frac{Y}{\left((1-jZ_i)^2 - \alpha^{-2}Y^2\right)} \tag{A.27}$$

$$\bar{\epsilon}_3 = 1 - \frac{X}{(1+\alpha^{-1})(1-jZ_e)} - \frac{X}{(1+\alpha)(1-jZ_e)}. \tag{A.28}$$

In the limit where ions are considered stationary then $\alpha \to \infty, Z_i \to 0$ and the tensor elements become,

$$\bar{\epsilon}_1 = 1 - \frac{X(1-jZ_e)}{\left((1-jZ_e)^2 - Y^2\right)} \tag{A.29}$$

$$\bar{\epsilon}_2 = -\frac{XY}{\left((1-jZ_e)^2 - Y^2\right)} \tag{A.30}$$

$$\bar{\epsilon}_3 = 1 - \frac{X}{(1-jZ_e)}. \tag{A.31}$$

The electron collision frequency can be estimated from the electron temperature and density using the relation (e.g. [18]),

$$\nu_e \sim \frac{n_e}{T_e^{3/2}} \left(34 + 4.18 \log\left[\frac{T_e^3}{n_e}\right]\right) . \tag{A.32}$$

Returning to the wave equation (Eq. A.10) the normal modes of the plasma when $\mathbf{J}_{ext} = 0$ are determined by setting the determinant of the matrix operator equal to zero,

$$\left|\mathbf{kk} - k^2\mathbf{I} + \omega^2\mu_0\boldsymbol{\epsilon}\right| = 0. \tag{A.33}$$

With the background magnetic field in the z direction there is no loss of generality in defining,

$$\mathbf{k} = k_x\mathbf{e}_x + k_z\mathbf{e}_z = k\left(\sin\theta\mathbf{e}_x + \cos\theta\mathbf{e}_z\right) , \tag{A.34}$$

in the spherical k coordinate system (k, θ, ϕ) . When expanded out in k Eq. (A.35) takes the form,

$$A\eta^4 - B\eta^2 + C = 0 , \tag{A.35}$$

where $\eta = ck/\omega$ is the index of refraction and,

$$A = \bar{\epsilon}_1 \sin^2\theta + \bar{\epsilon}_3 \cos^2\theta = S\sin^2\theta + P\cos^2\theta , \tag{A.36}$$

$$B = \left(\bar{\epsilon}_1^2 - \bar{\epsilon}_2^2\right)\sin^2\theta + \bar{\epsilon}_1\bar{\epsilon}_2\left(1 + \cos^2\theta\right) = RL\sin^2\theta + PS\left(1 + \cos^2\theta\right) \tag{A.37}$$

$$C = \bar{\epsilon}_3\left(\bar{\epsilon}_1^2 - \bar{\epsilon}_2^2\right) = PRL . \tag{A.38}$$

The solution to Eq. A.37 for $\eta(\theta)$ is,

$$\eta^2 = \frac{B \pm F}{2A} \ , \tag{A.39}$$

or, alternatively, the solution for $\theta(\eta)$ can be written,

$$\tan^2\theta = -\frac{P\left(\eta^2 - R\right)\left(\eta^2 - L\right)}{\left(S\eta^2 - RL\right)\left(\eta^2 - P\right)} \ , \tag{A.40}$$

where,

$$F^2 = B^2 - 4AC = \left(RL - SP\right)^2 \sin^4\theta + 4P^2D^2\cos^2\theta \ . \tag{A.41}$$

The general resonance condition $\eta \to \infty$ (i.e., the wavelength $\to 0$) determines the resonance angle θ_{res} through Equation (A.42),

$$\tan^2\theta_{res} = -\frac{P}{S} = -\frac{\bar{\epsilon}_3}{\bar{\epsilon}_1} \ . \tag{A.42}$$

From Eq. A.37 the propagation cutoff condition $\eta \to 0$ becomes

$$C = 0 \ . \tag{A.43}$$

For sake of completeness it is noted that the upper hybrid and lower hybrid resonance frequencies are defined as those frequencies at which $S = 0$. They are found from Eq. A.21 and A.12 to be,

$$\omega_{u(l)h} = \frac{\omega_{ce}^2 + \omega_{pe}^2 + \omega_{ci}^2 + \omega_{pi}^2}{2} \pm \frac{1}{2}\left[\left(\omega_{ce}^2 + \omega_{pe}^2 - \omega_{ci}^2 - \omega_{pi}^2\right)^2 + 4\omega_{pe}^2\omega_{pi}^2\right] \tag{A.44}$$

where the + root gives ω_{uh} and the − root gives ω_{lh}.

For a two component plasma with stationary ions the dispersion relation is often written in the Altar-Appleton-Hartree form [16],

$$\eta^2 = 1 - \frac{2\left(A - B + C\right)}{2A - B \pm \left(B^2 - 4AC\right)^{1/2}} \ . \tag{A.45}$$

Upon substitution of the definitions of the dielectric tensor components this becomes,

$$\eta^2 = 1 - \frac{2\omega_{pe}^2\left(\omega^2 - \omega_{pe}^2\right)/\omega^2}{2\left(\omega^2 - \omega_{pe}^2\right) - \omega_{ce}^2\sin^2\theta \pm \omega_{ce}\Delta} \ , \tag{A.46}$$

where,

$$\Delta = \left[\omega_{ce}^2\sin^4\theta + 4\left(\omega^2 - \omega_{pe}^2\right)^2\cos^2\theta/\omega^2\right]^{1/2} \ . \tag{A.47}$$

REFERENCES

[1] Wang, T. N. C. and T. F. Bell, Radiation resistance of a short dipole immersed in a cold magnetoionic medium, Radio Sci., 4, 167-177, 1969.

[2] Mittra, R. and G. A. Deschamps, Field solution for a dipole in a cold anisotropic medium, in Symposium on Electromagnetic Theory and Antennas, part 1, edited by E. C. Jordan, pp. 495-512, Pergamon Press, New York, 1963.

[3] Huang, X., and B. W. Reinisch, Excited spherical waves in unbounded cold magnetoplasma and applications in radio sounding, Radio Sci., 47, RS0L08, doi:10.1029/2011RS004940, 2012.

[4] Mlodnosky, R. F. and O. K. Garriott, The v.l.f. admittance of a dipole in the lower ionosphere, paper presented at the International Conference on the Ionosphere (London), Inst. of Phys. and Phys. Soc., Dorking, UK, 1962.

[5] Song, P., B.W. Reinisch, V. Paznukhov, G. Sales, D. Cooke, J.-N. Tu, X. Huang, K. Bibl, I. Galkin, High-voltage antenna-plasma interaction in whistler wave transmission: Plasma sheath effects, JGR, 112, A03205, doi:101029/2006JA011683, 2007.

[6] Tu, J., P. Song and B. W. Reinisch, Plasma sheath structures around a radio frequency antenna, J. Geophys. Res., 113, A07223, doi:10.1029/2008JA013097, 2008.

[7] Paznukov, V. V., G. S. Sales, K. Bibl, B. W. Reinisch, P. Song, X. Huang and I. Galkin, Impedance characteristics of an active antenna at whistler mode frequencies, JGR, 115, doi:10.1029/2009JA014889, 2010.

[8] Chevalier, T. W., U. S. Inan and T. F. Bell, Terminal Impedance and Antenna Current Distribution of a VLF Electric Dipole Antenna in the Inner Magnetosphere, IEEE Trans. Antennas and Propagation, 58, 8, 2454-2468, 2008.

[9] Chevalier, T. W., U. S. Inan and T. F. Bell, Fluid simulation of the collisionless plasma sheath surrounding an electric dipole antenna in the inner magnetosphere, Radio Sci., 45, RS1010, doi:10.1029/2008RS003843, 2010.

[10] Davis, V.A., M.J. Mandell, Spacecraft Charging Modeling – Nascap-2k, Section 5, AFRL-RV-PS-TR-2012-0209, 2012.

[11] Balmain, K.G., The Impedance of a Short Dipole Antenna in a Magnetoplasma, IEEE Trans. Antennas and Propagation, 12, 5, 605-617, 1964.

[12] Carpenter, D. L., and R. R. Anderson, An ISEE/Whistler Model of Equatorial Electron Density in the Magnetosphere, J. Geophys. Res, 97, A2, 1097-1108, 1992.

[13] International Geomagnetic Reference Field, www.ngdc.noaa.gov/IAGA/vmod/igrf.html, 2019.

[14] Su, Yi-J., et al., DSX Project Data Management Plan, Revision 2, AFRL Space Vehicles Directorate, 8 Aug 2018.

[15] Balanis, C.A., Antenna Theory, Chaps. 4 and 8, Wiley, Hoboken, 2016.

[16] Stix, T. H., Waves in Plasmas, American Institute of Physics, New York, 1992.

[17] Kutiev, I., K. Oyama and T. Abe, Analytical representation of the plasmasphere electron temperature distribution based on Akebono data, J. Geophys. Res., 107, A12, doi:10.1029/2002JA009494, 2002.

[18] Kelly, M. C., The Earth's Ionosphere, Appendix B., Academic Press, San Diego, 1989.

ACKNOWLEDGMENTS

The author wishes to thank Bodo Reinisch, Xueqin Huang (deceased), Michael Starks, Maria de Soria-Santacruz Pich and Jay Albert for useful discussions and encouragement.

This page intentionally left blank.

REPORT DOCUMENTATION PAGE

Form Approved
OMB No. 0704-0188

PLEASE DO NOT RETURN YOUR FORM TO THE ABOVE ADDRESS.

1. REPORT DATE *(DD-MM-YYYY)*	2. REPORT TYPE	3. DATES COVERED *(From - To)*
27/05/2020	Project Report	

4. TITLE AND SUBTITLE

VLF Far-field Radiation from a Linear Dipole Antenna Immersed in a Plasma: Baseline Model for DSX

5a. CONTRACT NUMBER

FA8702-15-D-0001

5b. GRANT NUMBER

5c. PROGRAM ELEMENT NUMBER

6. AUTHOR(S)

G.P. Ginet

5d. PROJECT NUMBER

5e. TASK NUMBER

5f. WORK UNIT NUMBER

7. PERFORMING ORGANIZATION NAME(S) AND ADDRESS(ES)

Lincoln Laboratory, MIT
244 Wood Street
Lexington, MA 02421-6426

8. PERFORMING ORGANIZATION REPORT NUMBER

95-0002

9. SPONSORING/MONITORING AGENCY NAME(S) AND ADDRESS(ES)

Air Force Research Laboratory/RVBX
3550 Aberdeen Ave, SE
Kirtland AFB, NM 87117-5776

10. SPONSOR/MONITOR'S ACRONYM(S)

AFRL

11. SPONSOR/MONITOR'S REPORT NUMBER(S)

12. DISTRIBUTION/AVAILABILITY STATEMENT

Distribution Statement A. Approved for public release. Distribution is unlimited

13. SUPPLEMENTARY NOTES

None

14. ABSTRACT

One of the prime objectives of the Demonstrations and Science Experiment (DSX) satellite mission is to determine the efficiency of injecting power into the magnetosphere at Very Low Frequencies (VLF) from an in-situ dipole antenna. A baseline VLF antenna radiation model for DSX has been developed using the stationary phase, far-field approximation to obtain a solution to the Green's function for the electric and magnetic fields driven by the antenna current in the limit of cold-plasma linear response theory. Estimates of the wave vectors and Poynting flux are output on the surface of a sphere of constant radius assuming a homogeneous plasma. The input antenna currents can either be specified from the data or derived from an impedance relation with the antenna voltages. An example impedance function, that of Balmain [11], is given and results generated for parameters typical of the DSX plasma environment. The intent of the model is to serve as a baseline linear model to which DSX data can be compared, and the differences used to guide model improvement.

15. SUBJECT TERMS

16. SECURITY CLASSIFICATION OF:			17. LIMITATION OF ABSTRACT	18. NUMBER OF PAGES	19a. NAME OF RESPONSIBLE PERSON
a. REPORT	b. ABSTRACT	c. THIS PAGE			19b. TELEPHONE NUMBER *(Include area code)*
unclassified	unclassified	unclasssified	unclassified		

This page intentionally left blank.